



HAL
open science

Development and digital twin of an experimental opto-electrothermal bench in the perspective of thin films thermal characterization

Sébastien Peillon, Petru Notingher, Christophe Rodiet

► **To cite this version:**

Sébastien Peillon, Petru Notingher, Christophe Rodiet. Development and digital twin of an experimental opto-electrothermal bench in the perspective of thin films thermal characterization. International Journal of Thermal Sciences, 2022, 178, pp.107549. 10.1016/j.ijthermalsci.2022.107549 . hal-03643484

HAL Id: hal-03643484

<https://hal.science/hal-03643484>

Submitted on 22 Jul 2024

HAL is a multi-disciplinary open access archive for the deposit and dissemination of scientific research documents, whether they are published or not. The documents may come from teaching and research institutions in France or abroad, or from public or private research centers.

L'archive ouverte pluridisciplinaire **HAL**, est destinée au dépôt et à la diffusion de documents scientifiques de niveau recherche, publiés ou non, émanant des établissements d'enseignement et de recherche français ou étrangers, des laboratoires publics ou privés.



Distributed under a Creative Commons Attribution - NonCommercial 4.0 International License

Development and digital twin of an experimental opto-electrothermal bench in the perspective of thin films thermal characterization

Sébastien PEILLON^{1,2}, Christophe RODIET³ and Petru NOTINGHER².

¹EPF, 21 Boulevard Berthelot, 34000 Montpellier, France

²IES, Univ Montpellier, CNRS, Montpellier, France

³Université de Reims Champagne Ardenne, ITheMM EA 7548, 51097 Reims, France

Corresponding authors: sebastien.peillon@epfedu.fr; christophe.rodiet@univ-reims.fr

Abstract – This work aims to widen the application of the front Flash methods to dielectric materials with thermal conduction times ranging from seconds to a few tens of nanoseconds. In this perspective, the design and characteristics of an experimental opto-electrothermal bench are presented here: its principle is based on the Flash methods (short optical excitation) however combined with an electrothermal measurement. The development of direct models acting as digital twins of the bench is also described. They allow considering its electrothermal behaviour, by taking into account the 1D thermal diffusion in a multilayer sample and the non-ideal frequency response of the acquisition chain (signal conditioner and the measuring devices) according to the sample thermal dynamics – which is little discussed in the literature to the authors' knowledge. The methodology proposed here for the sizing and consideration of the acquisition chain can be applicable to other electrothermal measurements methods such as the 3ω methods.

Keywords: differential measurements, digital twin, Flash methods, opto-electrothermal bench, thermal characterization, thin films.

Nomenclature:

a	thermal diffusivity ($\lambda/(\rho c_p)$), $m^2 \cdot s^{-1}$	λ	thermal conductivity, $W \cdot m^{-1} \cdot K^{-1}$
C	electric capacitance, F	φ	heat flux density, $W \cdot m^{-2}$
c_p	specific heat capacity, $J \cdot kg^{-1} \cdot K^{-1}$	ϕ	heat flux density in the Laplace domain
E	battery voltage, V	ρ	density, $kg \cdot m^{-3}$
Ef	effusivity ($\sqrt{\lambda \rho c_p}$), $J \cdot K^{-1} \cdot m^{-2} \cdot s^{-1/2}$	σ	standard deviation
e	thickness, m	τ_{laser}	laser pulse duration, s
f	frequency, Hz	τ_{cd}	thermal conduction time (e^2/a), s
G	conductance, Ω^{-1}	θ	temperature in the Laplace domain
Im	imaginary part	<i>Subscript and superscript</i>	
j	imaginary unit	0	initial
\mathcal{L}	Laplace transform	adm	admissible

\bar{m}	mean	c	capacitive (model) or cable (resistance, inductance, conductance or capacitance)
nt	number of time points	$calc$	calculated
P	power, W	$comp$	compensation (capacitance)
p	Laplace variable	eq	equivalent
Q	energy, W	exp	experimental
R	electrical resistor, Ω	end	last (value)
\mathcal{R}	reflectance, %	f	Sample/layer (film) to characterize
Re	real part	i	index of elements
S	surface, m^2	int	internal (resistance)
T	temperature, $^{\circ}C$	$laser$	laser
t	time, s	m	mean (model) or maximum (value)
U, V	electric voltages, V	osc	oscilloscope (device)
\mathfrak{U}	electric voltage in the Laplace domain	p	common value of the Wheatstone bridge resistors (R_0, R_2, R_3, R_4)
Var	variance	r	transducer (sensor/strip)
w	angular frequency ($2\pi f$), rad	s	shunt (resistance)
X	sensitivity	si	semi-infinite (model)
Z	electric impedance in Laplace domain	th	theoretical
<i>Greeks symbols</i>		v	variable
α	thermal coefficient, K^{-1}	*	reduced value
β	parameter		absolute value or modulus (for complex numbers)
ε	emissivity		
ϵ_{abs}	absolute error		
ϵ_{rel}	relative error, %		
$\epsilon_{rel,max}$	maximum relative error, %		
Λ	mean free path, m	bold:	vector

1. Introduction

Flash methods are widely used for the thermal characterization of materials ([1]–[4]). Yet, they are commonly restricted to $\sim 0.1\text{ m}$ thick materials ([5], [6]), thus limiting the characterization of low conduction times ones. To face this issue, it is required adjusting the characteristic times of both the excitation pulse (Dirac condition in time) and the temperature sensor (rapidity/delay), which is typically an infrared one to benefit from the non-invasive nature of optical methods. However, the use of optical sensors does not necessarily imply non-invasive measurements anymore for the characterization of thin films: their possible semi-transparency properties often require the use of an opaque coating to absorb and transmit the optical excitation [7]. Moreover, thin films short thermal time responses are a challenging issue that involves measuring high-frequency signals. Those high frequencies can then degrade the behaviour and sensitivity of the measuring systems (electronic components), which can result in a modification of the signal time slope or a low signal-to-noise ratio. All these aspects lead to the use of specific methods adapted to thin film thermal characterization [5]: either electrothermal ones such as the 3ω methods ([8], [9]) or optical ones like the FDTR/TDTR (Frequency/Time Domain ThermoReflectance) ([10]–[12]), both requiring a metal deposit.

This work aims to further develop a “hybrid” method still little documented ([13]–[16]). Its principle is based on the Flash methods (short optical excitation), however combined here with an electrothermal measurement of a thin metallic film. It therefore benefits from some advantages of the Flash methods: in particular, the simplicity of the thermal models to implement (a mere 1D diffusion model can be considered) and covering a wide range of thermal conduction times and conductivities. Two main objectives are pursued in this paper.

The first objective is to present the design and characteristics of the experimental opto-electrothermal bench designed to extend the applicability of the front Flash methods to dielectric materials with thermal conduction times ranging from seconds to a few tens of nanoseconds. Therefore, it has the potential to cover a wider range of conduction times than the methods mentioned earlier. It includes low thermal conductivity materials, such as polyethylene (thermal conductivity of about $0.5 \text{ W}\cdot\text{m}^{-1}\cdot\text{K}^{-1}$, [17]–[19]) or glass (thermal conductivity of about $1 \text{ W}\cdot\text{m}^{-1}\cdot\text{K}^{-1}$), but also high thermal conductivity ones such as aluminium nitride (AlN, thermal conductivity of around $100 \text{ W}\cdot\text{m}^{-1}\cdot\text{K}^{-1}$ with the possibility to exceed $250 \text{ W}\cdot\text{m}^{-1}\cdot\text{K}^{-1}$, [9], [20]–[22]) or diamond (thermal conductivity of around $2000 \text{ W}\cdot\text{m}^{-1}\cdot\text{K}^{-1}$). In this paper, the focus is on the intermediate range of $1 \text{ W}\cdot\text{m}^{-1}\cdot\text{K}^{-1}$ to $\sim 100 \text{ W}\cdot\text{m}^{-1}\cdot\text{K}^{-1}$ corresponding to the study of glass and AlN samples.

The second objective is to develop direct models that can act as digital twins of the developed bench and allow considering its electrothermal behaviour (thermal diffusion of the sample and non-ideal frequency response of the acquisition chain to its thermal dynamic). The resulting models will be useful for the subsequent implementation of the parameter estimation procedure (as simulation and inversion models for the characterization of an effective thermal conductivity or diffusivity). In this paper, thermal models are deliberately simplified for the benefit of a first approach in considering and identifying the impact of the acquisition chain on the measured signal – which is little discussed in the literature to the authors’ knowledge. The development of these thermal models will be the subject of subsequent studies (with due consideration to interface thermal resistances [6], [23]). Note that the methodology exposed here to obtain the electrothermal models can be extended to other electrothermal measurement methods.

This work will therefore address the following aspects. First, the proposed setup of the characterization bench is exposed ([13], [16]) with its associated acquisition chain. An idea of the frequency range held by the signals to be measured is also given, as a correct sizing of the bench depends on it (section 2). The frequency response of the acquisition chain is indeed dependent on the thermal dynamic of the sample. Thus, the implementation of simplified thermal models is studied. The spatial characteristics of the laser (optical excitation) are first

investigated to aim for the validation of a 1D thermal diffusion in multilayer samples. The introduction of simplified 1D models follows, based on a quadripolar formulation and considering the experimental time shape of the laser excitation (section 3). It is then possible to establish the electrothermal models related to the previously introduced acquisition chain, while justifying its design. A sensitivity study of the Wheatstone bridge is proposed in respect with the involved transducer to determine the optimal configuration of measurement. Furthermore, the use of a differential probe and its frequency response is discussed afterward in comparison with pseudo-differential measurements methods. To do so, the distortions occurring on the measured signal are implemented in the thermal modelling, resulting in electrothermal models adapted to various measuring devices (section 4). First experimental results are finally proposed on a glass sample to illustrate in first approximation the non-idealities of the acquisition chain (section 5).

2. Experimental bench and associated issues

To determine the effective thermal conductivity λ_f of a (thin) sample, an inverse method is coupled with measurements over time of the temperature of an opaque metallic layer (in our case, aluminium – Al). This layer, used as a transducer, is deposited on top of the dielectric thin sample to be characterized (which can be on a substrate), resulting in a multilayer system. Studies conducted on this paper consider materials with either a low (glass – Sample n°1) or high (AlN – Sample n°2) thermal conductivity value, as the latter have a wider frequency spectrum (see later in this section) that can affect the acquisition chain.

Parameters used for numerical studies are given in Table 1.

	λ [$W \cdot m^{-1} \cdot K^{-1}$]	ρc_p [$J \cdot m^{-3} \cdot K^{-1}$]	a [$m^2 \cdot s^{-1}$]	e [μm]	τ_{cd} [s]
Transducer - Al	120 ([11], [24])	$2.4 \cdot 10^6$	$5 \cdot 10^{-5}$	0.2 ($\approx 10\Omega$ [25])	$0.8 \cdot 10^{-9}$
Sample n°1 – Glass	1		$6 \cdot 10^{-7}$	1000	1.7
Sample n°2 - AlN	92 [20]		$3.8 \cdot 10^{-5}$	5000	0.7

Table 1. Properties of studied materials. $a = \lambda/(\rho c_p)$, $\tau_{cd} = e^2/a$.

The metallic layer (transducer) is an element of a balanced Wheatstone bridge where it is acting as an electric resistor (see Figure 1). Various shapes of aluminium metallic transducers are proposed in Figure 2 to tend to respect 1D thermal diffusion assumption in the sample (width larger than the thickness, weakly intrusive with regard to its conduction time, ...) and

electrical constraints (admissible power, bridge sensibility, ...) further exposed respectively in sections 3 and 4.1. After heating with a short (~ 10 ns) laser pulse, the thermoresistive effect of the transducer is used to determine its thermal evolution ΔT_r , induced by diffusion in the sample. Main characteristics of devices used (including the laser [26]) are displayed in Figure 3.

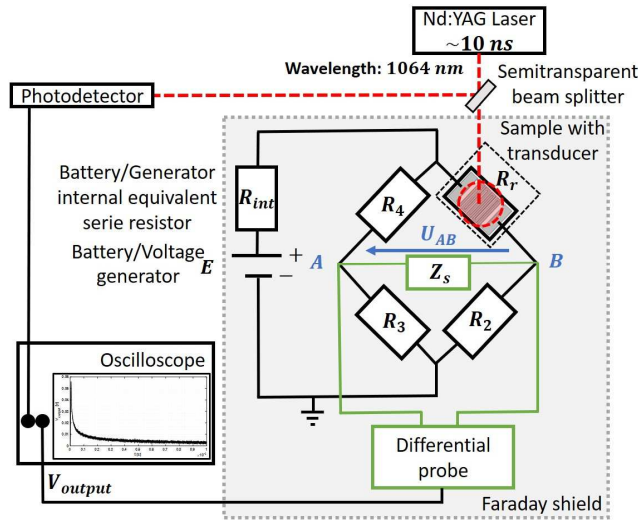


Figure 1. Schematic of the experimental opto-electrothermal method setup (a differential probe acts as the measuring device, but will be compared to other devices in section 4.2)

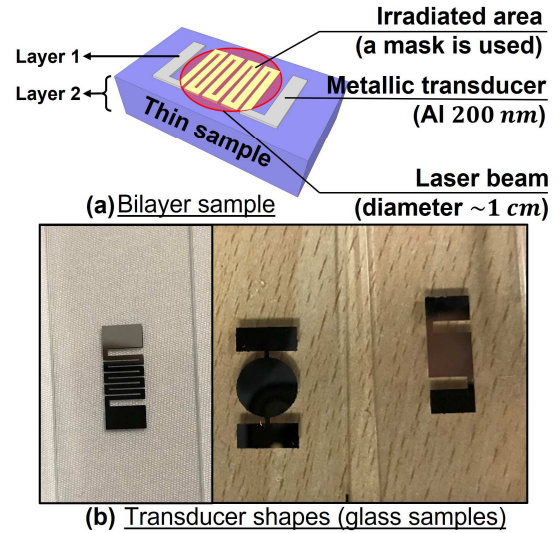


Figure 2. (a) Schematic of a bilayer sample (serpentine transducer shape). (b) Proposed transducer shapes (from left to right: serpentine, serpentine disc, disc, square inscribed in the disc)

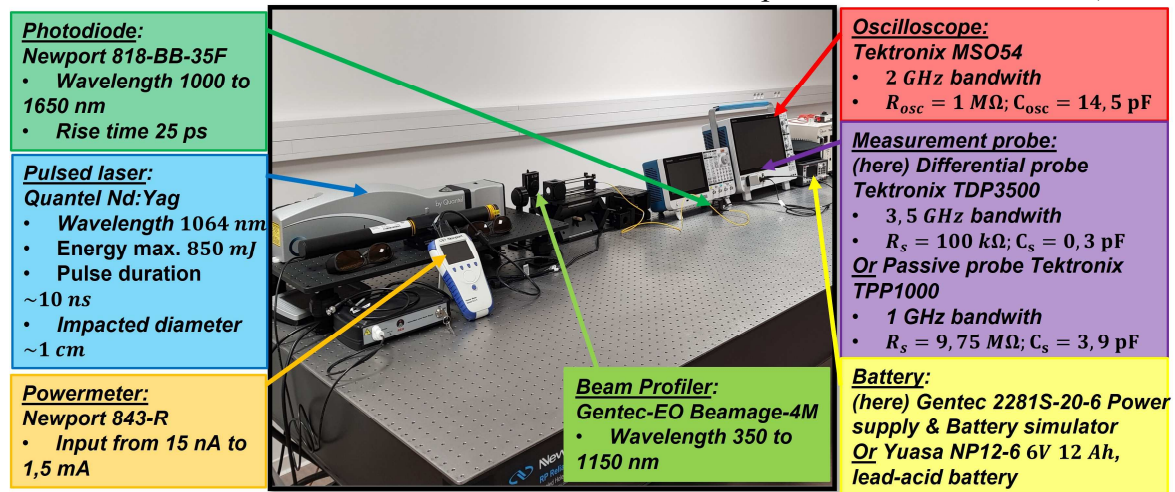


Figure 3. References of some of the developed opto-electrothermal bench devices

Measurements of the time-varying Wheatstone bridge voltage $U_{AB}(t)$, designated as $V_{output}(t)$ at the oscilloscope (see Figure 1), allow to obtain the electrical resistance of the metallic strip $R_r(T_r)$, and then its temperature variations $\Delta T_r(t)$. Indeed, the following relation can be used as a first approximation (for $\Delta T_{r,max} \leq 10$ °C):

$$R_r(T_r) = R_0(1 + \alpha_r \Delta T_r) = R_0 + \Delta R_r(T_r) \quad (1)$$

where $\Delta T_r(t) = T_r(t) - T_r(t_0)$ and with $\alpha_r \approx 3.7 \cdot 10^{-3} K^{-1}$ (the aluminium thermal coefficient value used for simulations [27]).

Temporal evolution of the measured signal $V_{output}(t)$ depends for one part on the thermal diffusion in the sample (section 3). In this aspect, the temporal shape of the laser excitation is of importance due to its significant influence on the diffusion during the pulse duration, as highlighted in Figure 4 for an AlN sample. Heat flux modelling used for this example are fittings of the experimental time shape of the laser excitation measured by a photodiode [28], based on several expressions presented in section 3.2 (with the parameters values used). In the case where the heat flux time-shape is not precisely known (*i.e.* not measured), it may be necessary to study the performance of various modelling of this heat flux in the perspective of a model reduction (involving a reduced number of parameters, thus reducing numerical instabilities for instance – see section 4.2.2).

It is pointed out in Figure 5 that the time of maximum temperature is influenced by the heat flux time shape, including when pulse duration is rigorously of the same length ($\tau_{laser} = 10 ns$ for all heat flux modelling in Figure 5), as well as by the sample conduction time (illustration for glass and AlN samples whose conduction times τ_{cd} are indicated in Table 1).

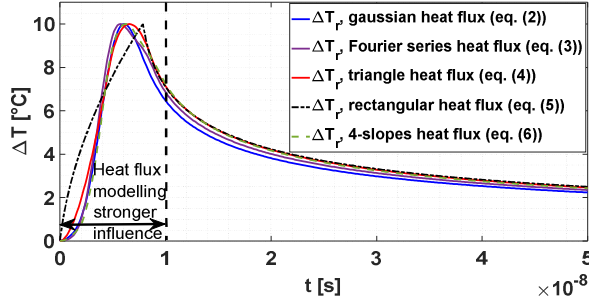


Figure 4. Influence of the experimental heat flux modelling on the thermal diffusion of an AlN sample (Sample n°2, “ T_m^{si} ” model, see eq. (9) in section 3.3)

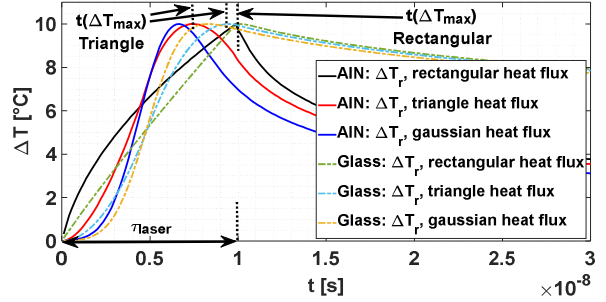


Figure 5. Heat flux time shape influence on the time of the maximum temperature (heat flux duration $\tau_{laser} = 10 ns$, “ T_m^{si} ” model)

Furthermore, the measured signal $V_{output}(t)$ is also affected by the acquisition chain (section 4), which includes a modification of the time of the maximum temperature previously mentioned. Indeed, the thermal response dynamic of the sample measured through the acquisition chain is experimentally altered by non-idealities of electronic components performances at high frequencies [29].

It is then useful to evaluate an upper limit of those frequencies for a proper sizing of the acquisition chain. In this perspective, a Discrete Cosine Transform decomposition (DCT) is conducted on the thermal response of an AlN thin sample (material with the highest thermal dynamic among the two studied, see section 3.3). In this example, a semi-infinite monolayer

behaviour of the sample is considered: this model provides the highest spectral composition as later highlighted in Table 3, while being representative of the limit (ideal) case where the transducer influence tends to be negligible – by reducing its thickness and/or enhancing its conductivity. The experimentally collected temporal shape of the laser excitation is used for this illustration (fitted using a 4-slopes expression detailed in section 3.2). The results are displayed in Figure 6: the highest frequency f_m allowing a good reconstruction of the signal is found in the frequency range of $\sim 600 \text{ MHz}$, with a maximum relative error $|\epsilon_{rel,max}| = \max\left(\left|\frac{\epsilon_{abs}(t)}{\max(\Delta T)}\right|\right) \leq 1\%$, where $\epsilon_{abs}(t)$ is the difference between the full-spectrum reconstructed signal and the filtered one from the frequency f_m . The associated reconstructed signal is displayed in Figure 7. A comparison with the DCT of the AlN sample while considering the Al transducer influence (thus resulting in a bilayer system) is also provided in Figure 6 (see section 3.3 for the thermal modelling used) and later discussed in this section.

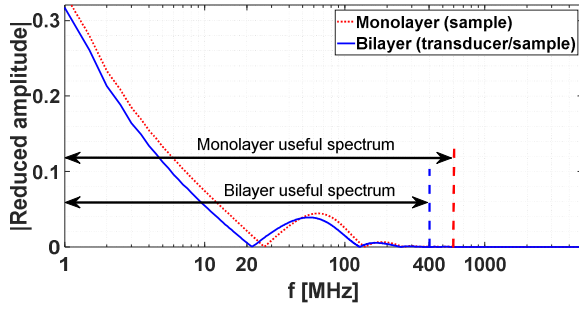


Figure 6. DCT of an AlN semi-infinite monolayer thermal signal (AlN – Sample $n^{\circ}2$, experimentally fitted 4-slopes heat flux shape). A comparison with the DCT of an AlN semi-infinite signal considering the transducer contribution (bilayer model, " T_m^{si} ") is provided.

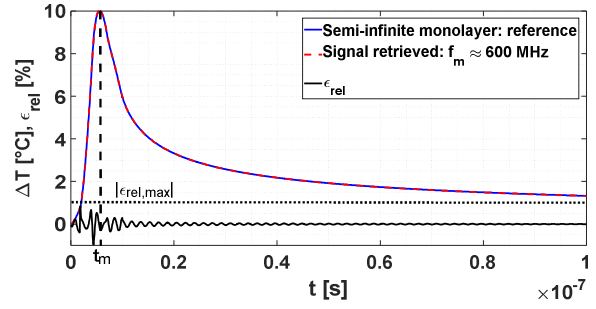


Figure 7. Temporal signal of an AlN semi-infinite monolayer thermal signal (AlN – Sample $n^{\circ}2$, experimentally fitted 4-slopes heat flux shape), reconstructed by inverse DCT

Maximum relative error $|\epsilon_{rel,max}|$ committed on the reconstruction for given maximum frequencies f_m are given in Table 2. Those frequencies correspond to visible bounces on the spectral decomposition of the monolayer thermal signal in Figure 6.

f_m [MHz]	$ \epsilon_{rel,max} $ [%]
~ 30	~ 60
~ 150	~ 10
~ 300	~ 3

Table 2. $|\epsilon_{rel,max}|$ obtained on the reconstructed signal after DCT for given frequencies f_m (complete signal of an AlN semi-infinite monolayer with a 4-slopes heat flux, see Figure 6)

and Figure 7)

Comparison with a - semi-infinite monolayer - glass sample is also given in Table 3 and shows a slightly lower f_m (~ 550 MHz compared to ~ 600 MHz previously). However, this frequency is further reduced when the contribution of the transducer to the thermal diffusion is considered (bilayer system with transducer on sample), as highlighted in Figure 6 (for the AlN sample) and Table 3 (see section 3.3 for the thermal modelling used). It is also reduced when only considering the relaxation phase (*i.e.* cooling phase) of the signal. This last aspect, highlighted in Figure 7 by observing lower values of $\epsilon_{rel}(t)$ in the cooling phase of the signal ($t \in [t_m; 1 \mu s]$), suggests lower distortions caused by the acquisition chain on this part, as it will be highlighted in section 4.2.

Conditions	Material	f_m [MHz]	f_m [MHz]
		Complete signal	Relaxation phase
4-slopes heat flux, semi-infinite monolayer	Glass	~ 550	~ 300
	AlN	~ 600	~ 300
4-slopes heat flux, bilayer (" T_m^{si} " model)	Glass	~ 250	~ 150
	AlN	~ 400	~ 300

Table 3. Frequency f_m allowing a good reconstruction ($|\epsilon_{rel,max}| \leq 1\%$) of either the complete signal or its relaxation/cooling phase after DCT

Those frequency ranges are to be considered for a proper sizing of the measuring bench (especially of the measuring devices) to avoid frequency-dependent distortions.

The reliability of the experimental set-up is also to be considered to minimize variability on the measurements (section 5). For differential measurements ($U_{AB}(t)$), methods using a differential probe are often more expensive than pseudo-differential ones (where a mathematical difference between two measurements signals is performed). In return, it provides a better reliability of measurements by limiting the number of devices, connections and cables lengths, while usually benefitting of higher performances at high frequencies (see section 4.2 and [30], [31]).

Some assumptions are made throughout this work. Variations in the bridge resistors ohmic values (other than the metallic transducer) are considered negligible due to their low self-heating by Joule effect (maximum temperature coefficient of a resistor is 80 ppm/ $^{\circ}C$ [32]) and their low tolerance value (1% [32]). They can also be assumed non-inductive and non-capacitive thanks to their design, contrarily to the measuring device (oscilloscope by itself or measuring probes) which presents a frequency-dependent behaviour. It is also assumed that initial stability of the acquisition chain is reached at the starting time of experiment t_0 [s]

corresponding to the time of laser impulse (probes and circuit are under voltage and heating temperature of the transducer after Joule effect – due to circuit powering up - is attained).

3. Thermal modelling

The behaviour of the measured electrothermal signal displayed on the oscilloscope depends on the thermal diffusion in the sample (ΔT_r , see eq. (1)), which interacts with the frequency response of the measurement chain. Thus, it is important to use a direct model that can accurately describe the thermal evolution of the sample, while potentially involving a minimum number of parameters (parsimony principle).

In this regard, uniformity of the thermal excitation provided by the laser must be experimentally checked (section 3.1). Indeed, in addition to the use of a transducer whose width (1 cm, *i.e.* the impact diameter of the laser pulse) is much larger than its thickness (200 nm, see Figure 2 (b)) and a short study time range (1 μ s), it permits considering a 1D transient heat transfer (section 3.3). It should be noted that the transducer thickness is about 10Λ , with Λ the mean free path of the heat carriers (see reference [25] for aluminium), to stay in a diffusive regime.

Moreover, time-shape distribution of the laser is experimentally retrieved (section 3.2). This thermal excitation appears in the Laplace domain as a factor of a transfer function in the thermal models used (section 3.3). Therefore, it directly impacts the dynamic of the thermal signal (see Figure 4 and Figure 5).

3.1. Heat flux spatial distribution

Since an average heat temperature measurement is performed on the transducer, it is sought to ensure that the average 1D transfer can be considered identical to the global 1D transfer and does not require additional considerations of heat sink terms due to edge effects (non-homogenous boundary conditions due to potential non-negligible lateral losses compared to the in-thickness heat transfer) or to local non-linearities caused by a strong spatial non-homogeneity of the excitation. In that regard, a spatial uniformity check of the laser excitation is performed with a Gentec-EO Beamage-4M Profiler, whose spectral range is adapted to the laser wavelength of 1064 nm [26].

3D and 2D profiles are displayed at the top and bottom of Figure 8, respectively. Figure 9 shows 1D profiles along the two lines (black and dotted red) displayed in the 2D profile of Figure 8.

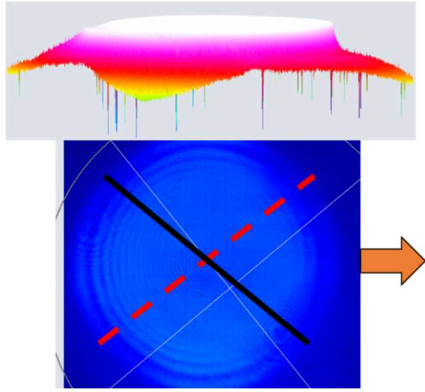


Figure 8. 3D (top) and 2D (bottom) spatial distribution profiles of the laser excitation

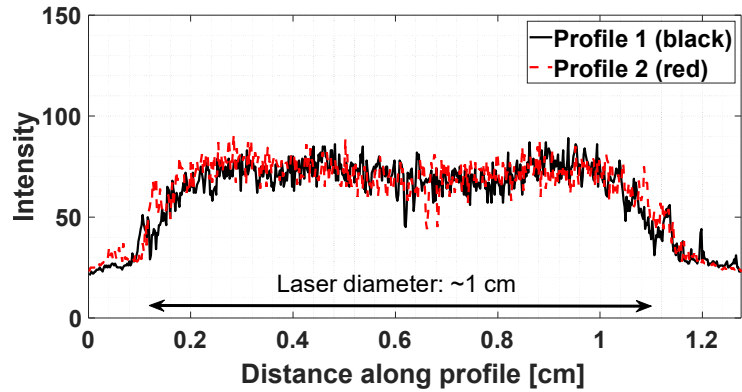


Figure 9. 1D spatial distribution profiles of the laser excitation along the two lines (black and dotted red) displayed in the bottom image of Figure 8

Spatial distribution at the centre of the excitation can be considered globally uniform (flat front laser). In addition to the previously presented hypothesis (study time, transducer design), this tends to allow the use of 1D thermal models.

3.2. Heat flux time shape

The thermal diffusion of the sample being affected by the temporal shape of the laser excitation $\varphi_{laser}(t)$ (see Figure 4 and Figure 5), it must be experimentally retrieved and properly modelled to be considered with the transfer function of the thermal diffusion modelling (developed in section 3.3).

The experimental laser time shape is thus collected with a Newport 818-BB-35F (fibre) photodetector [28] and represented in solid black line in Figure 10. A voltage plateau attributed to a malfunction of the photodiode is observed from ~ 10 ns to ~ 30 ns: this was confirmed by subsequent new, but noisier, measurements (lower experimental signal to noise ratio) performed with photodetectors of similar performances – Newport 818-BB-35 [33] and EOT ET-3600 [34] – that did not exhibit this behaviour. The signal is thus manually arranged here (for illustrative purposes only) to correct this distortion, resulting in the blue signal displayed in Figure 10. A new photodiode will be needed for the characterization procedure.

The tendency of the reduced “corrected” signal ($U_{laser}^*(t) = U_{laser}(t) / \max(U_{laser}(t))$) is then fitted with a least square method associated with a regularized Levenberg-Marquardt descent algorithm [35]. Various functions, expressed either in temporal or Laplace domain, are tested to find a simple yet accurate modelling of the heat flux temporal signal involving a minimum of parameters (and thus preventing as much as possible the appearance of potential numerical instabilities).

Figure 11 displays fittings realized in the temporal domain with a gaussian function (red

curve, described by eq. (2)) and a 400-terms real Fourier series (blue curve, described by eq. (3)). This last fitting was realized with a ‘‘Simple real Fourier series approximation’’ algorithm [36].

$$\textbf{Gaussian: } U_{laser,gauss}(t) = be^{-\frac{(t-\mu)^2}{2\sigma^2}} \quad (2)$$

with $b = \frac{K}{\sigma\sqrt{2\pi}}$, where $\sigma = 1.6 \text{ ns}$ and $\mu = 4.5 \text{ ns}$ are respectively the standard deviation and the mathematical expectation estimated simultaneously with $K = 3.5 \cdot 10^{-9}$ (amplitude coefficient, see Figure 11).

$$\textbf{Fourier series: } U_{laser,Fourier}(t) = \frac{A_0}{2} + \sum_{k=1}^{400}(A_k \cos(kt) + B_k \sin(kt)) \quad (3)$$

where A_k , B_k , and A_0 are the fitted coefficients of the Fourier series [36]. Once these coefficients are obtained, it is possible to freely reconstruct the fitted signal on the time of the experiment by using eq. (3). However, it is necessary to remove any sinusoidal variations appearing after τ_{laser} (highlighted in Figure 11) due to the periodic behaviour of the Fourier series.

If the gaussian function allows a good approximation of the heat flux temporal behaviour, the Fourier series is the most accurate of the two.

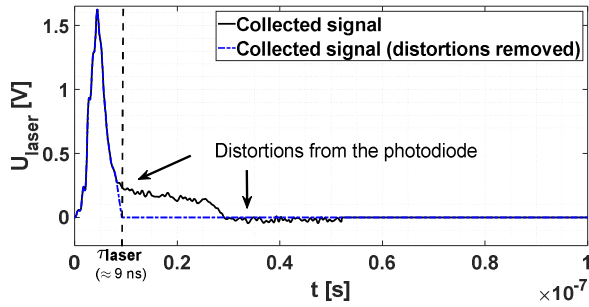


Figure 10. Experimental laser time-shape signal collected with a photodiode and proposed correction of distortions

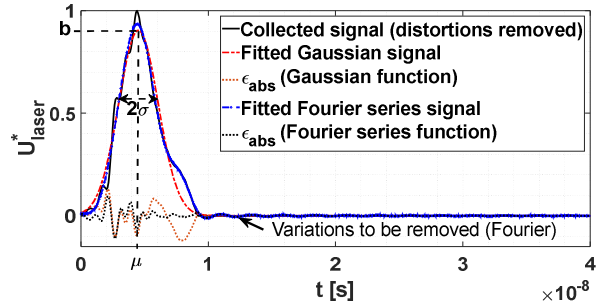


Figure 11. Fitted functions on the reduced laser time-shape signal, expressed in the temporal domain (zoomed)

A quadrupole formulation being used for the thermal models developed in section 3.3, tests are carried out with functions expressed in the Laplace domain ($\mathfrak{U}_{laser}(p) = \mathcal{L}(U_{laser}(t))$, see eq. (8) in section 3.3 for the Laplace transform definition). It will result in simpler expression of the thermal and electrothermal models developed later in this paper.

Figure 12 displays fittings performed with two functions: a triangle function (red curve described by eq. (4), implying three introduced parameters), which seems to be the global tendency of the heat flux behaviour, and a rectangular function (blue curve described by eq.

(5)), one of the usual functions in Laplace domain benefitting from very few (two) parameters to introduce. The inverse Laplace transform is carried out thanks to a numerical De Hoog algorithm [37]. Note that the Laplace transform of the Gaussian expression is not used here as it does not converge easily in the time domain when $t \rightarrow 0$ s (as highlighted in [38]).

$$\text{Triangle: } \mathfrak{X}_{laser,tr}(p) = \frac{U_m}{\tau_m p^2} (1 - e^{-\tau_m p}) + \frac{U_m}{(\tau_m - \tau_{laser}) p^2} (e^{-\tau_m p} - e^{-\tau_{laser} p}) \quad (4)$$

where $U_m = 0.84$, $\tau_m = 4.45$ ns and $\tau_{laser} = 8.69$ ns are estimated (see Figure 12).

$$\text{Rectangular: } \mathfrak{X}_{laser,rec}(p) = \frac{U_m}{p} (1 - e^{-\tau_{laser} p}) \quad (5)$$

where $U_m = 0.44$ and $\tau_{laser} = 7.87$ ns are estimated (see Figure 12).

While the rectangular function is clearly not adapted to describe the heat flux temporal behaviour, it is not so obvious for the triangle function. A more accurate model based on a 4-slopes interpolation function is thus proposed in comparison in Figure 13. Its expression is of the following form:

$$\begin{aligned} \text{4-slopes: } \mathfrak{X}_{laser,4slopes}(p) = & \frac{U_1}{\tau_1 p^2} (1 - e^{-\tau_1 p}) + \frac{U_1 - U_m}{(\tau_1 - \tau_m) p^2} (e^{-\tau_1 p} - e^{-\tau_m p}) - \\ & \frac{U_2 - U_m}{(\tau_m - \tau_2) p^2} (e^{-\tau_m p} - e^{-\tau_2 p}) + \frac{U_2}{(\tau_2 - \tau_{laser}) p^2} (e^{-\tau_2 p} - e^{-\tau_{laser} p}) \end{aligned} \quad (6)$$

where estimated values are indicated in Figure 13.

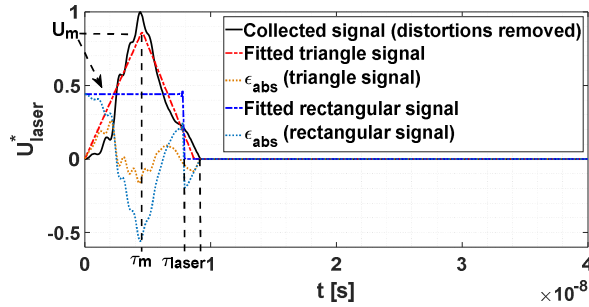


Figure 12. Fitted functions on the reduced laser time-shape signal, expressed in the Laplace domain (zoomed)

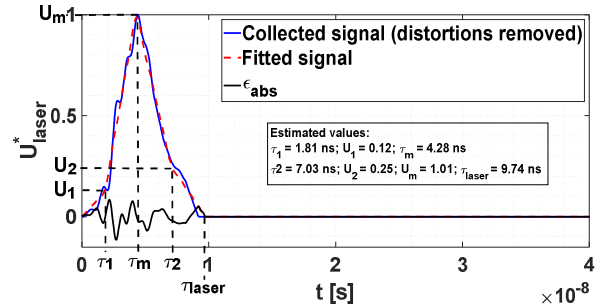


Figure 13. Fitted 4-slopes interpolation function expressed in the Laplace domain on the reduced laser time-shape signal (zoomed)

This 4-slopes expression is clearly more adapted than the triangle one to describe the heat flux behaviour. In addition, using temporal domain heat flux expressions will imply to perform multiple convolutions to obtain the thermal and electrothermal signals (see eq. (9) to eq. (14) and eq. (23) to eq. (26)). The choice is thus made to use this Laplace domain 4-slopes expression, using the values indicated in Figure 13 for the next numerical studies.

Influence of this heat flux temporal shape compared to the Fourier series fitted one (presenting fewer differences with the collected signal, see Figure 11) is highlighted in section 3.3 on the thermal diffusion of a glass and an AlN sample. A good agreement is observed over the whole thermal signal ($|\epsilon_{rel,max}| \leq 1.6\%$), indicating a fine performance of the 4-slopes fitting.

However, this expression involves many parameters (seven parameters) to introduce, which can generate numerical instabilities (see section 4.2.2). In those cases, the triangle function, presenting fewer parameters (three parameters), is appealing to continue working in the Laplace domain. The influence of these two heat flux expressions (4-slopes and triangle) on the thermal diffusion is compared in the context of the materials studied in this paper in section 3.3. It will be shown that using any of these expressions only lead to a small difference between the two thermal signals while focusing on their relaxation phase ($|\epsilon_{rel,max}| \leq 3\%$).

Finally, the expression of $\phi_{laser}(p)$ in the Laplace domain can be obtained as follows:

$$\phi_{laser}(p) = Q(1 - \mathcal{R}(Al))\mathfrak{A}_{laser}^*(p)/S \equiv \varphi_m \mathfrak{A}_{laser}^*(p) \quad (7)$$

with Q the incident energy, $\mathcal{R}(Al)$ the reflectivity of the aluminium (Al) transducer at 1064 nm and where φ_m represents the power absorbed by the aluminium transducer per surface unit.

Experimentally, the time shape of the laser impulse is measured during each experiment by deflecting part of the laser beam using an optical beam routing.

3.3. Sample thermal modelling

Now as spatial uniformity is assessed and as the heat flux time shape is recovered, a comparison of two different 1D models is proposed in this section to determine the evolution of the metallic strip temperature $\Delta T_r(t)$.

The first one considers temperature changes according to the metallic transducer thickness and then its mean temperature (eq. (9)) [16]. The second model, more valid as the transducer is thin and sufficiently good thermal conductor, considers it as an isothermal layer (eq. (10)). Unlike the first model, it does not imply the knowledge of the transducer conductivity property (which can be thickness-dependent) and will therefore simplify the use of the model for the first tests on experimental data (see section 5). Its validity is checked in first approximation in this section.

As for the sample, it can be considered as a semi-infinite layer thanks to the short study time

(1 μ s) compared to the materials conduction times τ_{cd} (indicated in Table 1, section 2). It is pointed out that interface thermal resistance between the transducer and the sample (existing due to the lattice mismatch, rugosity, interstitial third body, ...) is not considered here and will be the subject of subsequent studies.

Furthermore, thermal exchanges with the surroundings can be neglected thanks to a weak emissivity of the metallic transducer ($\varepsilon_r < 0.1$), temperature rise ($\Delta T \leq 10$ °C) and short-time measurement (1 μ s).

The problem can then be modelled using a quadrupole expression [39] expressed in the Laplace domain, whose transform is defined as:

$$\theta_i(p) = \mathcal{L}(T_i(t) - T_\infty)(p) = \int_0^{+\infty} (T_i(t) - T_\infty) e^{-pt} dt \quad (8)$$

In the case of a “mean temperature” transducer (see Figure 14), the Laplace transform of the difference between the transducer and the surrounding medium temperatures $\theta_r(p)$ (see eq. (1)) can be written as:

$$\theta_m^{si} \text{ model: } \theta_r(p) = \frac{A_r + B_r G_{\infty,f}}{C_r + G_{\infty,f} D_r} \phi_{laser}(p) \quad (9)$$

with $\phi_{laser}(p) = \varphi_m \mathfrak{A}_{laser}^*(p)$ (see section 3.2). Coefficients in eq. (9) are detailed in Figure 14.

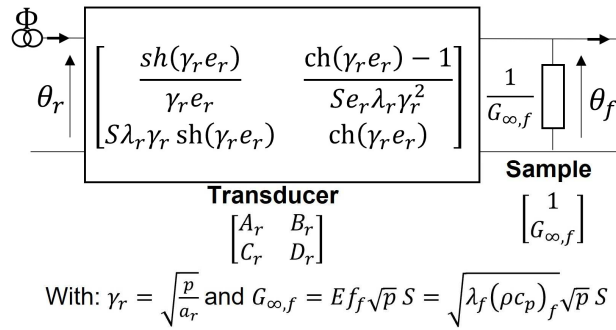


Figure 14. Quadrupole schematic of the heat diffusion in a bilayer medium (the “mean temperature” of the transducer is considered [16] on a semi-infinite sample)

By modelling the transducer as a capacitive medium (isothermal layer, see Figure 15), the diffusion can be modelled by the following quadrupole form:

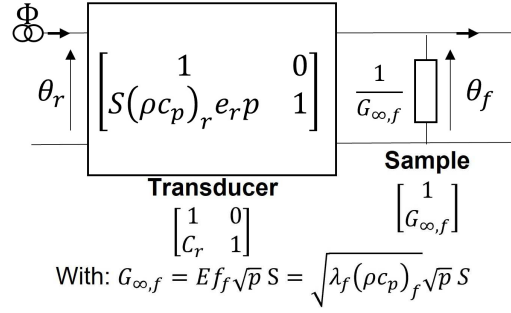


Figure 15. Quadrupole schematic of the heat diffusion in a bilayer medium (a capacitive modelling of the transducer is considered on a semi-infinite sample)

The model then degenerates into:

$$\theta_c^{si} \text{ model: } \theta_r(p) = \frac{1}{C_r + G_{\infty,f}} \phi_{laser}(p) \quad (10)$$

with $\phi_{laser}(p) = \varphi_m \mathfrak{A}_{laser}^*(p)$ (see section 3.2). Coefficients in eq. (10) are detailed in Figure 15.

By applying a numerical inverse Laplace transform [37] on eq. (9) and eq. (10), thermal models “ T_m^{si} ” and “ T_c^{si} ” models are respectively obtained in the temporal domain.

Figure 16 thus displays the thermograms of the investigated materials (see Table 1 in section 2) obtained using those thermal models (capacitive “ T_c^{si} ” or “mean temperature” “ T_m^{si} ”) until 1 μ s. The greater dynamic response of the AIN signal is clearly distinguished. Also, the bias on the aluminium transducer modelling increases as the conductivity of the sample is higher, as highlighted in Figure 17. It is thus not very pregnant for the low conductivity glass sample ($|\epsilon_{rel,max}^{complete}| \approx 2\%$), contrarily to the AIN one ($|\epsilon_{rel,max}^{complete}| \approx 21\%$). However, this bias is reduced when focusing on the relaxation phase ($|\epsilon_{rel,max}^{relaxation}| \approx 0.5\%$ for the glass sample and $|\epsilon_{rel,max}^{relaxation}| \approx 12\%$ for the AIN one). It will allow (in first approximation) the use of a capacitive modelling of the transducer to reduce the number of parameters in first experimental tests on experimental signals conducted on glass samples in section 5. It is pointed out that the relative maximum error is reduced such that $|\epsilon_{rel,max}^{relaxation}| \leq 1\%$ for the AIN sample when $t \geq 36.5$ ns.

Deposited energy was adjusted in all studied cases to attain a 10 °C temperature elevation.

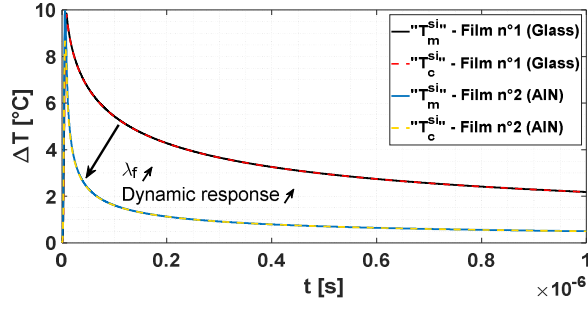


Figure 16. Thermograms of studied materials (time study of 1 μ s)

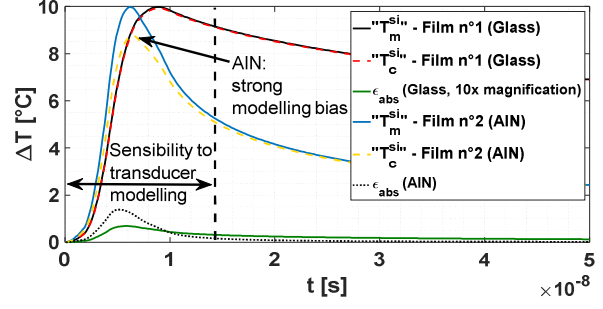


Figure 17. Biases on the thermal modelling of the transducer (zoomed)

In addition, the influence of the heat flux time shape modelling on the dynamics of the thermal signals is highlighted for the glass sample in Figure 18 and the AlN sample in Figure 19 for the " T_m^{si} " model: from the most accurate to the least accurate heat flux modelling, the thermal signals based on a Fourier series (resulting from the convolution of eq. (3) with the transfer function of eq. (9) multiplied by the factor φ_m described in eq. (7)), a 4-slopes (see eq. (6)) and a triangle (see eq. (4)) heat flux expressions are thus compared here.

To do so, the relative error $\epsilon_{rel}(t) = \epsilon_{abs}(t) / \max(\Delta T)$ is computed in each case, where $\epsilon_{abs}(t)$ is the difference between the thermal signal considering the most accurate heat flux modelling and that considering the least one, and $\max(\Delta T)$ is the maximum temperature of the signal with the most accurate heat flux modelling. A higher maximum relative error $|\epsilon_{rel,max}|$ is systematically observed during the heating phase, as reported in Table 4. Thus, the triangle heat flux modelling can be considered in first approximation on the relaxation phase of the signal, including when compared to the Fourier series heat flux modelling (in both cases, $|\epsilon_{rel,max}| \leq 0.6\%$ for the glass sample and $|\epsilon_{rel,max}| \leq 3\%$ for the AlN one). Finally, the small differences between the complete signals based on the 4-slopes and the Fourier series heat flux modelling can be noted ($|\epsilon_{rel,max}| < 2\%$ for both materials) and indicate in first approximation a good reliability of the 4-slopes modelling.

Similar results were found with the " T_c^{si} " model in the same configurations. It is also reminded that the influence of the others modelling of the heat flux time shape on the thermograms (gaussian and rectangular expressions proposed in section 3.2) is illustrated in Figure 4 on the thermal diffusion of an AlN sample.

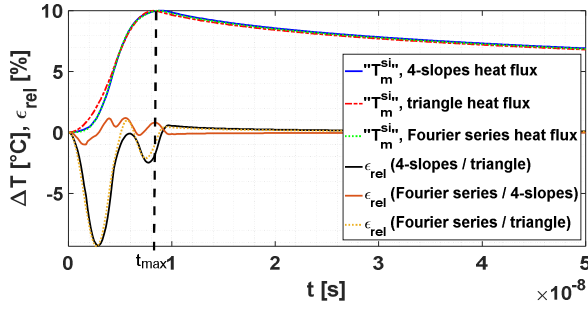


Figure 18. Comparison of heat flux time shape influence on the thermal signal of a glass sample (Sample n^o1)

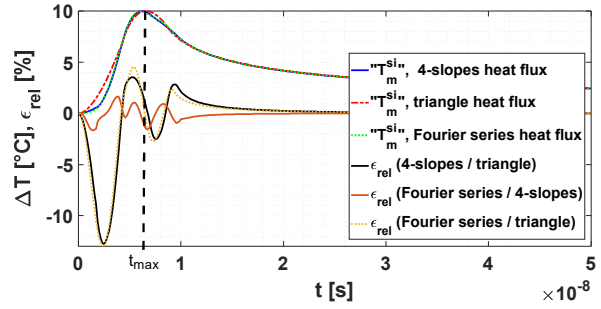


Figure 19. Comparison of heat flux time shape influence on the thermal signal of an AlN sample (Sample n^o2)

Signals based on a ...	Material	$ \epsilon_{rel,max} $ Complete signal	$ \epsilon_{rel,max} $ Relaxation phase
4-slopes heat flux compared to triangle heat flux	Glass	9.3 %	0.6 %
	AlN	12.8 %	3 %
triangle heat flux compared to Fourier series heat flux	Glass	9.3 %	0.5 %
	AlN	13 %	2.7 %
4-slopes heat flux compared to Fourier series heat flux	Glass	1.2 %	0.7 %
	AlN	1.7 %	1.5 %

Table 4. Comparison of thermograms based on the " T_m^{si} " model using several heat flux time shape modellings introduced in section 3.2. Similar results are obtained with the " T_c^{si} " model

4. Acquisition chain sizing

4.1. Optimization of the Wheatstone bridge

4.1.1. Bridge sensitivity

Experimentally, the variation of the transducer temperature ΔT_r (see section 3.3) is provided by the variation of the - out of balance - voltage of a balanced Wheatstone bridge. Several advantages come from the use of differential measurements methods. As such, it is possible to cancel out the offset voltage – thus obtaining a full scale on the oscilloscope – and to minimize signal saturation and clipping problems. Moreover, effects of non-ideal behaviour of resistors (capacitive and inductive) due to high frequencies are reduced. Some influencing factors are also compensated, like variations of the power supply (potentially unstable at high frequency and sensitive to electromagnetic noise, generated by the laser impulse for instance) – this effect is illustrated later in this section.

Several measurement methods exist for measuring the bridge differential voltage $U_{AB}(t)$ [31], resulting in various expressions of this voltage. Two methods are investigated in this

paper and illustrated in Figure 20, where E is the generator (or battery) voltage and R_{int} its internal equivalent series resistance whose influence is studied in section 4.1.2.

The first method is a “differential probe measurements” technique (involving a differential probe, see Figure 20 (a)), while the second one is a pseudo-differential measurements (also called an “A Minus B”) method where a mathematical difference between a first (V_1) and a second (V_2) signal voltage is computed (by the oscilloscope or post-measurements). This last pseudo-differential method is performed either with two passive single-ended probes (with each probe ground lead referenced to ground points M_1 and M_2 , see Figure 20 (b)) or, in a downgraded way, with two direct cable connections from the oscilloscope to the bridge circuit (see Figure 20 (c)). Other options are possible but not investigated here (one of them is the use of active probes [40]).

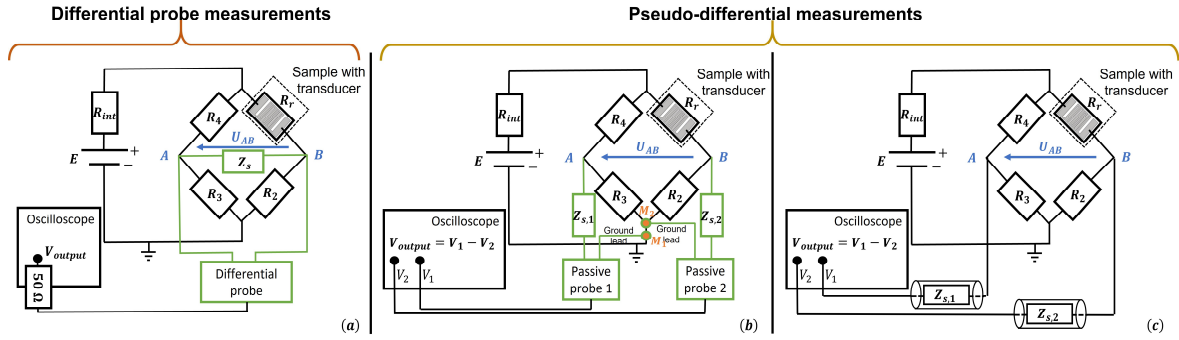


Figure 20. Schematics of the Wheatstone bridge differential voltage measurement, using a differential probe (a), two passive measurement probes (b) or two direct connections to the oscilloscope (c). The last two cases are studied examples of the so-called pseudo-differential measurement methods (mathematical subtraction of two signals). Note that V_{output} , V_1 and V_2 are distinguished from respectively U_{AB} , V_A and V_B

In comparison with the differential probe method, pseudo-differential methods are affordable (*i.e.* cheaper than differential ones) and easy-to-access approaches that, however, can only provide good results if probes, ground leads, cables and oscilloscope channels are well matched to maximize the common mode rejection ratio [30]. In this aspect, differential probe measurements are often more reliable by providing a better common mode rejection ratio at higher frequencies, as it will be highlighted on the experimental measurements (see section 5).

In both cases, special care must be given to the probes characteristics (bandwidth, input capacitance and resistance, ..., see section 4.2) in accordance to the expected frequency spectrum of the signal to be measured (as shown in section 2) to minimize the influence of the acquisition chain on the measurements.

In the case of differential probe measurements (Figure 20 (a)), the voltage $U_{AB}(t)$ can be defined in the Laplace domain by:

$$\mathfrak{A}_{AB}(p) = \frac{E Z_S(p)(R_3 Z_r(p) - R_4 R_2)}{\mathfrak{Y}(p) \cdot (R_3 + R_4)(Z_r(p) + R_2) + R_{int}[Z_S(p)(Z_r(p) + R_2 + R_3 + R_4) + (R_4 + Z_r(p))(R_3 + R_2)]} \quad (11)$$

where $\mathfrak{Y}(p) = Z_S(p) + \frac{R_3 R_4}{R_3 + R_4} + \frac{Z_r(p) R_2}{Z_r(p) + R_2}$ and $Z_r(p) = \mathcal{L}(R_r(t)) = R_0 + \mathcal{L}(\Delta R(t))$ is the transducer impedance (“Sample with transducer” in the schematics in Figure 20, see eq. (1)). $Z_S(p)$ is the input impedance of the measuring device, whose impact and modelling are further studied in section 4.2.1 (consideration of the connection to the oscilloscope by a 50 Ω termination is overlooked in this expression due to its low value compared to probe impedance value ~ 100 k Ω , see section 4.2.1):

$$Z_S(p) = \frac{R_S}{1 + R_S C_S p} \quad (12)$$

In the case of pseudo-differential measurements (Figure 20 (b) and (c)), the voltage $U_{AB}(t) = V_A(t) - V_B(t)$ is expressed in Laplace domain by another expression:

$$\mathfrak{A}_{AB}(p) = \frac{Z_r(p)[R_A(p)(E - V_{M,2}) + R_4(V_{M,1} - V_{M,2})] - R_B(p)R_4(E - V_{M,1}) + R_{int}(V_{M,1} - V_{M,2})(Z_r(p) + R_4)}{Z_r(p)(R_A(p) + R_4) + R_B(p)(R_4 + R_A(p)) + R_{int}(R_A(p) + R_B(p) + R_4 + Z_r(p))} \quad (13)$$

where $R_A(p) = \frac{R_3 Z_{s,1}(p)}{R_3 + Z_{s,1}(p)}$ and $R_B(p) = \frac{R_2 Z_{s,2}(p)}{R_2 + Z_{s,2}(p)}$, with $Z_{s,1}(p)$ and $Z_{s,2}(p)$ the input impedance of the channel 1 (V_1) and channel 2 (V_2) respectively: when using passive probes, it includes their impedance and their connection to the oscilloscope (see Figure 20 (b) and eq. (18) in section 4.2.1), or in the case of direct connections to the oscilloscope, the impedance of the cables and their connection to the oscilloscope (see Figure 20 (c) and eq. (17) in section 4.2.1). Further details are given on how electric connections to the oscilloscope are realized in section 4.2.1. $V_{M,1}$ and $V_{M,2}$ are respectively the ground leads voltages of the channel 1 and channel 2 passive probes which, in theory, are of the same value and null.

When using direct connection cables, it is pointed out that the ground used is the internal reference of the oscilloscope (grid-related ground), which can differ of the ground circuit [30].

Assuming that passive probes (or direct connection cables) are well matched (same model device or connection cables, *i.e.* $Z_{s,1}(p) \approx Z_{s,2}(p) \approx Z_S(p)$, described by eq. (17) and eq. (18)) as well as ground leads voltages (meaning that ground lead cables type, length, connection and positioning are similar, *i.e.* $V_{M,1} \approx V_{M,2} \approx 0$ V), this expression can be simplified as follows:

$$\mathfrak{U}_{AB}(p) = \frac{E Z_s(p)[Z_s(p)(R_3 Z_r(p) - R_4 R_2) + R_2 R_3 (Z_r(p) - R_4)]}{[R_3 R_4 + Z_s(p)(R_3 + R_4)][Z_r(p)R_2 + Z_s(p)(Z_r(p) + R_2)] + R_{int}[R_2 R_3 (Z_r(p) + R_4) + Z_s(p)R_C(p)]} \quad (14)$$

where $R_C(p) = (R_3 + R_2)(Z_r(p) + R_4) + 2R_2 R_3 + Z_s(p)(Z_r(p) + R_2 + R_3 + R_4)$.

This expression will be used in the paper's continuation, as some parameters of eq. (13) are unknown ($V_{M,1}$, $V_{M,2}$, $Z_{s,1}(p)$, $Z_{s,2}(p)$). Their influence is reduced by experimentally using the same measuring device on each channel (see section 4.2).

Additionally, it is reminded that bridge compensation, allowing nullifying the initial offset ($U_{AB}(t_0) = 0 V$), is achieved if the following relation is verified at the initial time t_0 :

$$R_3 R_r(t_0) - R_4 R_2 = 0 \quad (15)$$

This bridge compensation effect on symmetrical voltage variations (*i.e.* variations on each branch) is illustrated in Figure 21. The differential voltage $U_{AB}(t)$ is computed in two cases. The first one considers a balanced bridge (*i.e.* $\forall i \in \{2; 3; 4\}, R_i = R_r(t_0) = R_p$, thus satisfying eq. (15)) while using differential probe measurements (blue signal, see eq. (11)) or pseudo-differential measurements (dotted brown signal, see eq. (14)). The second case considers an unbalanced bridge (in the given example, $R_{\{2;3;4\}} \neq R_r(t_0)$), thus displaying an initial voltage offset for differential probe measurements (red signal, see eq. (11)) and pseudo-differential measurements (dotted blue signal, see eq. (14)). The generator voltage E (green signal) is also represented. It is defined here as a direct (constant) voltage ($E_{dc} = 1 V$) with added variations $E_{ac}(t)$ that simulates unstable behaviour of the power supply (or approximately cables lead effects) at a given frequency ($E = E_{dc} + E_{ac}(t) = E_{dc} + e^{-t/\tau} \sin(2\pi f t)$, with here $\tau = 10^{-7} s$ a time constant and the frequency $f = 57 MHz$).

This behaviour can be induced by an external noise (laser electromagnetic noise) or cables exhibiting transmission lines conduct (ringing noise, see [31], [41], [42]). Note that Z_s and R_{int} are set for this study such that they do not influence the differential measurement (large shunt impedance compared to the bridge resistors, *i.e.* $Z_s \rightarrow +\infty$, and $R_{int} = 0 \Omega$).

It then appears that the differential voltage stays cleared from distortions with a balanced bridge. It is not the case of an unbalanced bridge configuration, which highlights the importance of the initial balance of the bridge to reduce the effects of such voltage variations. It should be noted that in the unbalanced bridge case, amplitude of the distortions depends on the values of the resistors and is further reduced while the initial balancing difference tends towards zero (*i.e.* $(R_3 R_r(t_0) - R_4 R_2) \rightarrow 0$).

Next, it might be important to optimize the sensitivity of the bridge to improve the experimental signal-to-noise ratio. The bridge sensitivity to the transducer resistance

variation defined by $X_{\Delta R}(t) = \frac{\partial U_{AB}(t)}{\partial \Delta R}$ is thus studied in Figure 22, for several configurations presented in Figure 23 with respect to the expressions of $U_{AB}(t)$ established in eq. (11) and eq. (14). R_v stands for the resistors whose values are changed for this numerical study and $E = 1 V$ (direct voltage) is merely acting as a sensitivity multiplier. Again, Z_s is supposed to be an infinitely large impedance in comparison to the other resistors (influence highlighted in section 4.2) and $R_{int} = 0 \Omega$ (see section 4.1.2) to remove their contribution. In this case, sensitivity curves shown in Figure 22 are identical whether the measurement is performed with a differential (eq. (11)) or a pseudo-differential technique (eq. (14)) ($\epsilon_{abs,max} < 10^{-5} V$). Therefore, they are represented only once for readability; However, it will be highlighted that those sensitivities differ with respect to the input impedance $Z_s(p)$.

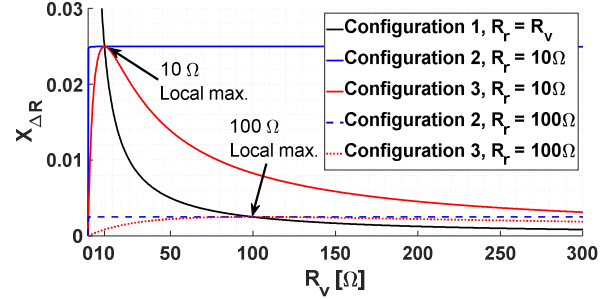
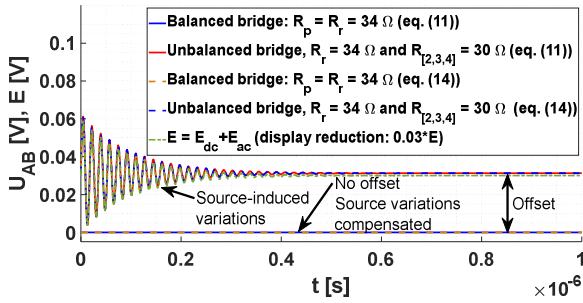


Figure 21. Influence of the generator voltage variations on the differential voltage for both differential probe and pseudo-differential measurements methods

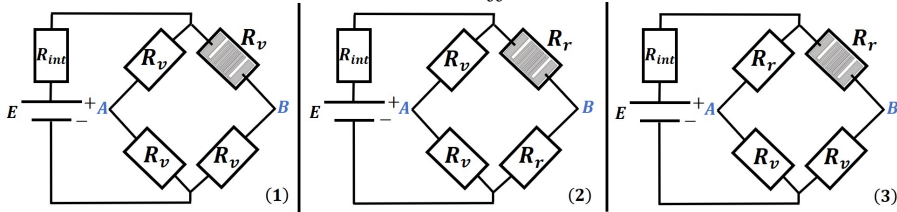


Figure 23. Studied bridge resistors configurations (configurations 1 to 3) - R_r and R_v resistors are here respectively fixed (r) and variable (v) values

Figure 22 highlights that an optimum sensitivity is found when all bridge resistors (*i.e.* R_p) are of the same value ($R_p = R_r$, noted as local maxima in the figure) and maximized when $R_p \rightarrow 0$. However, this does not consider the limited power provided by the generator ($P = E^2/R_p$), as well as the – low [32] - self-heating of the resistors.

Moreover, the bridge resistors can withstand a limited power (admissible power $P_{adm} \leq 30 W$ for resistors other than the transducer [32]). A minimum value of R_p must therefore be observed and can be determined using the following inequality:

$$R_p \geq \frac{E^2}{4P_{adm}} \quad (16)$$

In addition, the generator voltage E must be limited due to several considerations: by the measurement device input voltage limits (for instance, $E_{adm} < 10 V$ with the TDP3500 differential probe – see section 4.2 - to respect its maximum admissible common mode voltage [43]) or by the current intensity supported by the sample with transducer - and its connections).

If it appears beneficial to decrease the global value of the resistors to enhance the bridge sensitivity, thermal considerations limit this possibility, imposed by the heat transfer modelling (exposed in section 3.3) which requires that the transducer respects some constraints: metallic material, very low thermal conduction time $\tau_{cd,r}$, large width to the thickness ratio and thicknesses $e_r \ll e_f$, such that the transducer is weakly intrusive for the measurement and for the 1D assumption. Its geometry is then fixed (proposed geometries are presented in Figure 2 (b)) and consequently its initial resistance $R_r(t_0) = R_0$ (see eq. (1)).

Studies not presented here (with electrothermal finite element simulations and 4-wire type electrical measurements) allow envisaging R_0 values ranging from 10Ω to 100Ω . Thus, this range holds in the cases investigated in this paper, with the Wheatstone bridge resistors in configuration 1 (*i.e.* $R_p = R_r$, see Figure 23 (1)) to provide an optimal bridge sensitivity to transducer resistance variations ΔR .

4.1.2. Influence of the internal resistance of the generator

Furthermore, the bridge sensitivity is deteriorated by two more points: the measuring device influence (Z_s , investigated in the next section 4.2) and the internal resistance of the generator R_{int} .

As the latter increases, sensitivity of the bridge is reduced, as displayed in Figure 24 for discrete values of R_{int} . It is pointed out that the influence of R_{int} on the bridge sensitivity $X_{\Delta R}$ is similar whether the measurements are performed with differential or pseudo-differential techniques, which is highlighted by the overlapping of the corresponding curves in Figure 25). This sensibility decrease should be investigated. Indeed, if a 6 V Yuasa lead-acid battery (characteristics in Figure 3 and [44]) displays an internal impedance value of $\sim 8 m\Omega$ at 1 kHz, this value increases with respect to frequency [45]. A linear extrapolation of the behaviour exposed in the reference [45] would lead to a value of $\sim 600 \Omega$ at 600 MHz (see Figure 6 and Figure 7 in section 2). In this case, it greatly influences the sensibility of the Wheatstone bridge.

It is shown in Figure 25 that the degradation due to R_{int} can be considered negligible if the R_p/R_{int} ratio exceeds 20. This ratio should be maintained throughout all the time of

measurement of the signal.

In the paper's continuation, influence of R_{int} will be neglected due to the lack of accurate data in its high frequency-dependent behaviour (in low frequency, its influence can be overlooked).

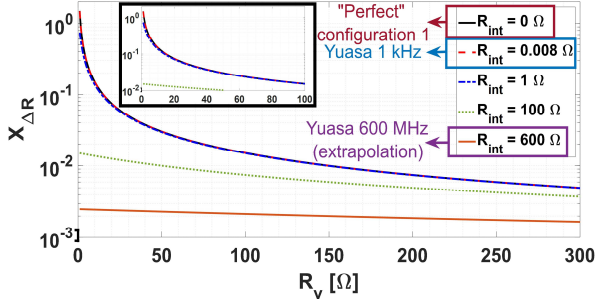


Figure 24. R_{int} impact on the bridge sensibility for $E = 6 V$ (Yuasa battery voltage) and $Z_s \rightarrow +\infty$ in Configuration 1 ($\forall i, R_i = R_p$)

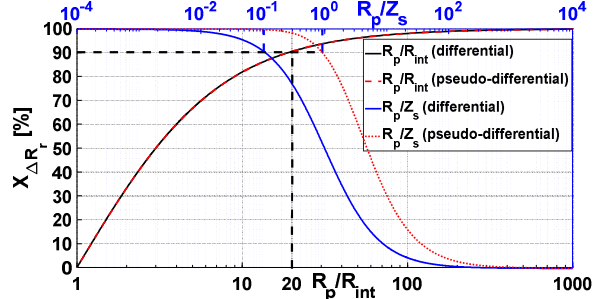


Figure 25. Influence of the ratios R_p/R_{int} and R_p/Z_s on the bridge sensibility $X_{\Delta R}$ attainable in Configuration 1 ($\forall i, R_i = R_p$). 100% is equivalent to Configuration 1 sensibility with $R_{int} = 0 \Omega$ and $Z_s \rightarrow +\infty$

4.2. Measuring device influence

4.2.1. Modelling and influence of the measuring devices

The bridge sensibility is further diminished by the influence of the measuring device impedance Z_s . Therefore, it is necessary to model its impact when acquiring the differential (measured) signal V_{output} displayed at the oscilloscope (see Figure 20).

Ideally, Z_s must be large (infinite) in comparison to the bridge resistors in order to avoid causing signal source loading and thus interfering with the measurements: R_p/Z_s ratio should be smaller than 10^{-1} when performing differential probe measurements (eq. (11)) and $9 \cdot 10^{-1}$ with a pseudo-differential technique (eq. (14)) to reach at least 90 % of the bridge sensibility without any source loading effects, as indicated in Figure 25.

Furthermore, this input impedance Z_s can be further modelled by eq. (12) in the case of measurement probes, using R_s and C_s – respectively the equivalent resistance and capacitance of the measuring device, usually given by the manufacturer. Low values of resistance R_s can affect the amplitude of the measured signal while the capacitance C_s , particularly important for high frequency signals, affects its rise time (it will be highlighted later in this section) ([29], [41]).

Moreover, these probes are connected to the oscilloscope, resulting in an additional influence to consider. The connection is usually performed either through a 50Ω (when using a differential probe) or a $1 M\Omega$ input termination (with passive probes or a direct cable

connection) and allows minimizing signal distortions caused by parasitic effects such as reflected signals (due to impedance mismatch, [41], [46]).

It results in three equivalent circuits for the measurements methods studied in this paper ([40], [47]). A schematic of these circuits is provided in Figure 26 for differential probes measurements and Figure 27 for pseudo-differential techniques, either with passive probes (Figure 27 (a)) or direct connections to the oscilloscope (Figure 27 (b)). R_{osc} and C_{osc} values, respectively the equivalent resistance and capacitance of the oscilloscope, are usually given by the manufacturer.

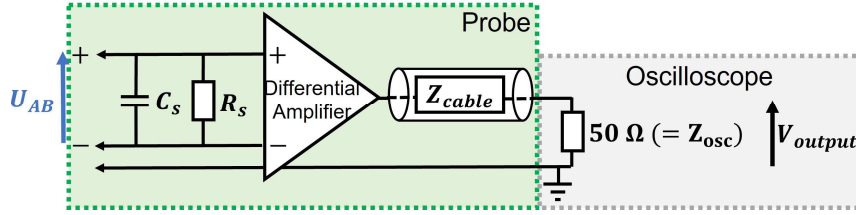


Figure 26. Schematic of the equivalent electrical circuit of the input impedance of a differential probe. The impedance matching is done via the probe cable (characteristic impedance of 50Ω). Based on [40]

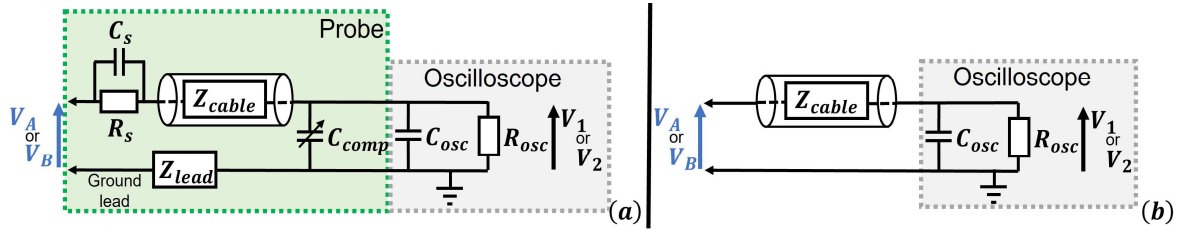


Figure 27. Schematics of the equivalent electrical circuit of the input impedance of one passive probe (a) and one direct cable connection to the oscilloscope (b). Based on [47]

Note that probes display an attenuation factor A_d due to the voltage divider thus realized ($V_1 \neq V_A$ for instance in Figure 27 (a)), allowing measuring signals of higher amplitude. The oscilloscope usually compensates this factor on the display. When using passive probes, it is determined - at low frequencies and approximately - by the voltage divider composed of the probe resistance R_s and that of the oscilloscope ($R_{osc} \approx 1 M\Omega$, see next paragraph). This implies that 10:1 probes usually show larger resistance values than 1:1 probes and thus cause less source loading issues. In the differential probe case, it is done through the differential gain of the amplifier (see Figure 26).

When considering the connection to the oscilloscope and the cable presence (which can possibly behave as transmission lines at high frequencies [42]), a new equivalent input impedance $Z_{s,i}(p)$ can be expressed for pseudo-differential measurements, where i refers to the oscilloscope channel used (channels 1 and 2, $i = \{1; 2\}$, see eq. (13)).

When using the oscilloscope directly with cables, this expression is:

$$Z_{s,i}(p) = Z_{cable,i}(p) + Z_{osc}(p) = \frac{Z_{cable,i}(p)(1+R_{osc}C_{osc}p)+R_{osc}}{1+R_{osc}C_{osc}p} \quad (17)$$

$$\text{where } Z_{osc}(p) = \frac{R_{osc}}{1+R_{osc}C_{osc}p}.$$

In the case of passive probes, it becomes:

$$Z_{s,i}(p) = \frac{R_{s,i}}{1+R_{s,i}C_{s,i}p} + Z_{cable,i}(p) + Z_{osc}(p) + Z_{lead,i}(p) \quad (18)$$

where $Z_{osc}(p) = \frac{R_{osc}}{1+R_{osc}(C_{osc}+C_{comp,i})p}$ and $Z_{lead,i}(p)$ is the impedance of the passive probe

ground lead wire. $C_{comp,i}$ is a variable capacitance adjusted by the oscilloscope during the probe calibration procedure usually performed - for each channel - prior to the measurements with a square wave of frequency $f = 1 \text{ kHz}$ (*i.e.* $\omega = 2\pi \cdot 10^3 \text{ rad}$). In particular, it compensates for the introduction of the probe capacitance (contrarily to the uncompensated cable capacitance when using a direct connection to the oscilloscope) by providing the suitable attenuation factor $A_{d,i}$ ([41], [47]).

Indeed, assuming that $p = j\omega$, $C_{comp,i}$ is defined at the 1 kHz frequency such that:

$$\text{Im} \left(\frac{Z_{osc}(j\omega)}{Z_{s,i}(j\omega)} \right) = 0 \quad (19)$$

It results in $Z_{osc}(j\omega)/Z_{s,i}(j\omega)$ the voltage divider transfer function - involved in eq. (25) and eq. (26) - a real number at this frequency.

The passive probe attenuation factor is then defined by:

$$A_{d,i} = \left| \frac{Z_{osc}(j\omega)}{Z_{s,i}(j\omega)} \right| \quad (20)$$

This factor is compensated by the oscilloscope with the attenuation value defined at 1 kHz such that $A_{d,i}^{1 \text{ kHz}} = A_{d,i}(\omega = 2\pi \cdot 10^3)$.

As illustrated in Figure 28 for a Tektronix TPP1000 passive probe (see later this section, $A_{d,i} \approx 1/10$), this factor is the same for all frequencies when cable $Z_{cable,i}(j\omega)$ and ground lead $Z_{lead,i}(j\omega)$ impedances have little to no influence (*i.e.* low frequency measurements, see blue curve). However, this is no longer the case at high frequency when an impedance of these elements is considered (see red curve with the example of a 50 Ω lossless cable); It results in an imperfect compensation – by the oscilloscope - of the attenuation factor at these frequencies.

To provide an example of these calculations in the simplified case when cable and ground

lead impedances are overlooked (*i.e.* $Z_{cable,i}(j\omega) = Z_{lead,i}(j\omega) = 0$), $C_{comp,i}$ and $A_{d,i}^{1kHz}$ can be defined by $C_{comp,i} = -\frac{R_{osc}C_{osc}-R_{s,i}C_{s,i}}{R_{osc}}$ and

$$A_{d,i}^{1kHz} = R_{osc} \frac{[1+(C_{comp,i}+C_{s,i}+C_{osc})(R_{s,i}w_{1kHz})^2 C_{s,i}]R_{osc}+R_{s,i}}{[1+(C_{comp,i}+C_{s,i}+C_{osc})^2(R_{s,i}w_{1kHz})^2]R_{osc}^2+2R_{osc}R_{s,i}+R_{s,i}^2}; \text{ with } w_{1kHz} = 2\pi \cdot 10^3 \text{ rad.}$$

In this paper, the frequency-dependent behaviour of cables for the differential and passive probes measurements is overlooked due to the lack of accurate data on the technical description of the probes (thus $Z_{cable}(p) = 0$). Consequently, it is assumed that values given by the manufacturer already include the probe cable input resistance and capacitance and that these are properly compensated at high frequencies (lossless cables at high frequencies). It is also assumed that the ground lead wire impedance of the passive probes is properly compensated ($Z_{lead,i}(p) = 0$).

However, for the method using direct connections to the oscilloscope which can be performed with commercial BNC cables (for instance), the behaviour of a 1 m coaxial cable is modelled, either as a $Z_{cable,i}(p) = 50 \Omega$ (for $i = \{1; 2\}$) resistive impedance (lossless cable) or a transmission line [42].

In this last case, $Z_{osc}(p)$ is defined in eq. (17) as:

$$Z_{osc}(p) = \frac{R_{osc}}{1+R_{osc}[G_c+(C_{osc}+C_c)p]} \quad (21)$$

with $C_c \approx 100 \text{ pF}$ and $G_c \approx 7 \cdot 10^{-22} \Omega^{-1}$ respectively the capacitance of the coaxial cable and the conductance of the cable dielectric insulation.

As for $Z_{cable,i}(p)$, it is defined as:

$$Z_{cable,i}(p) = R_c + L_c p \quad (22)$$

with $R_c \approx 17 \text{ m}\Omega$ and $L_c \approx 253 \text{ nH}$ respectively the resistance and the inductance of the cable.

The electric schematic of the equivalent input impedance in this case is given in Figure 29.

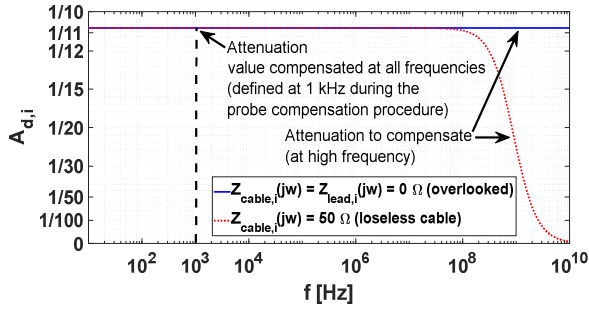


Figure 28. Influence of $Z_{cable,i}(j\omega)$ on the frequency dependent value of the attenuation factor $A_{d,i}$ realized by the voltage divider (TPP1000 passive probe). The oscilloscope compensates the value $A_{d,i}^{1\text{ kHz}}$ (set at 1 kHz) at all frequencies

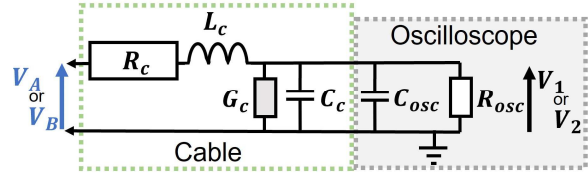


Figure 29. Schematic of the equivalent electrical circuit of the input impedance of one direct coaxial cable connection to the oscilloscope modelled as a transmission line [42]

With the modelling of Z_s exposed, the choice of the measuring device to perform the differential measurement can now be discussed. It is done here by comparing a differential probe (Tektronix TDP3500 [43]), adapted to high frequency until 3.5 GHz, to pseudo-differential measurements, either with two passive measuring probes (Tektronix TPP1000 [48]) dedicated to high frequencies until 1 GHz or with a high frequency (2 GHz) oscilloscope used on its own with direct connections by coaxial cables (example of the Tektronix MSO5 [49]).

Differentiation between these devices, other than their respective initial equivalent resistance and capacitance values (characteristics in Figure 3), depends on their bandwidth, hence on the deterioration of their characteristics at high frequencies. This deterioration is highlighted for their input impedance values, digitalized from their data sheet (black curves) in Figure 30 for the differential TDP3500 probe and Figure 31 for the passive TPP1000 probe. Resulting curves from manufacturer equivalent resistance and capacitance values are given (blue curves) along with the (red) curve resulting from the estimation of their values with a least-squares method [35]. A better fitting being obtained for the TDP3500 probe, a new value of capacitance C_s for this probe is chosen ($C_s = 0.49\text{ pF}$ instead of the manufacturer value $C_s = 0.3\text{ pF}$).

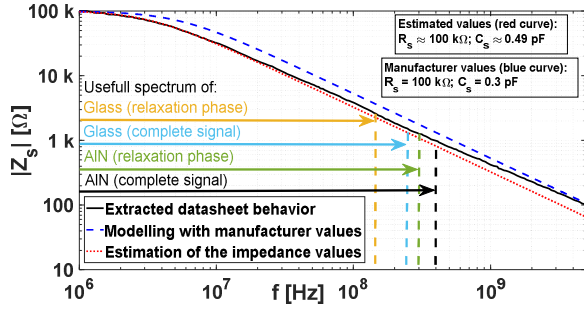


Figure 30. Frequency-dependent behaviour of the input impedance of the TDP3500 differential probe. Extracted data from [43].

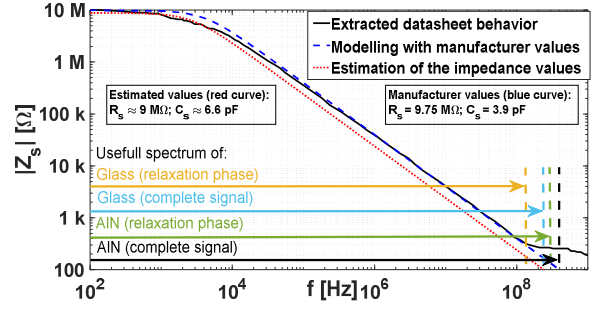


Figure 31. Frequency-dependent behaviour of the input impedance of the TPP1000 passive probe. Extracted data from [49].

Measuring devices also contribute to the amplification of the common mode voltage. Added to the differential voltage $U_{AB}(t)$ (see eq. (11) and eq. (14)), this parasitic voltage is eliminated to a greater or lesser extent depending on the device used and its bandwidth in the case of a differential probe (see section 4.2.2).

Thus, in the case of the differential probe, the voltage $V_{output}(t)$ measured by the measuring device is expressed in the Laplace domain as:

$$V_{output}(p) = A'_d(p) \mathfrak{A}_{AB}(p) \left(1 + \frac{1}{CMRR(p)} \frac{\mathfrak{A}_{cm}(p)}{\mathfrak{A}_{AB}(p)} \right) \quad (23)$$

with $\mathfrak{A}_{AB}(p)$ described by eq. (11) in section 4.1 - involving the input impedance of the differential probe $Z_s(p)$ (see eq. (12)) -, $CMRR(p)$ the common mode rejection ratio of the probe (a frequency-dependent performance given by the manufacturer, further investigated in

section 4.2.2) and the coefficient $A'_d(p) = \frac{Z_{osc}(p)}{Z_{cable}(p) + Z_{osc}(p)} A_d$ (A_d is the differential gain of

the differential probe and $Z_{osc}(p) = 50 \Omega$, see Figure 26), expressed in the Laplace domain.

The coefficient $A'_d(p)$ is compensated by the oscilloscope through proper probe compensation procedure at 1 kHz such that $A'_d(p) = A'_d = 1$. It is reminded that improper compensation of this attenuation at high frequency (similar to passive probes compensation procedure exposed earlier, see Figure 28) is not studied in this paper due to the lack of accurate data concerning the probes cable (modelling of $Z_{cable,i}(p)$). An illustration of this effect influence is however provided for passive probes later in this section.

As for the common mode voltage, it can be expressed in the Laplace domain as $\mathfrak{A}_{cm}(p)$ by:

$$\mathfrak{A}_{cm}(p) = \frac{E[Z_s(p)(R_3 Z_r(p) + R_2 R_4) + 2R_3 R_2 R_A(p)]}{2Z_r(p)[Z_s(p)R_4 + R_3 R_B(p)] + 2R_2[(Z_s(p) + Z_r(p))R_4 + R_3 R_A(p)] + 2R_{int}[R_A(p)(R_3 + R_2) + Z_s(p)R_C(p)]} \quad (24)$$

where $R_A(p) = Z_s(p) + R_4 + Z_r(p)$; $R_B(p) = Z_s(p) + R_4$ and $R_C(p) = Z_r(p) + R_4$. $Z_s(p)$ is described by eq. (12) defined in section 4.1.

In the case of pseudo-differential measurements, this common voltage existing on both bridge branches is theoretically suppressed by the mathematical difference (“A Minus B”) when the assembly is perfectly symmetrical: bridge symmetry, mismatch of ground leads lengths and positioning - which can result in a potential voltage difference of each probe grounds references (see eq. (13) with $V_{M,1}(p) \neq V_{M,2}(p)$) - or the non-ideal symmetry of the two passive probes frequency performances ($Z_{S,1}(p) \neq Z_{S,2}(p)$ in eq. (13)) are factors that contribute to the amplification of the common mode voltage.

It is difficult to quantify the quality of the common mode rejection in the pseudo-differential case. It depends on many unknown parameters such as ground leads cables composition (for transmission lines effects), their position (impacting values of $V_{M,1}(p)$ and $V_{M,2}(p)$), frequency-dependent performances and mismatch of each of the two passive probes, ... ([30], [42]). The voltage $V_{output}(t) = V_1(t) - V_2(t)$ in the Laplace domain is thus expressed here without consideration of this parasitic voltage for the pseudo-differential methods as:

$$V_{output}(p) = A'_{d,1}(p) \frac{(ER_A(p)+V_{M,1}R_4)(Z_r(p)+R_B(p))+R_{int}R_4[V_{M,1}(R_B(p)+R_4+Z_r(p))+V_{M,2}R_A(p)]}{(Z_r(p)+R_B(p))(R_4+R_A(p))+R_{int}(Z_r(p)+R_4+R_A(p)+R_B(p))} - A'_{d,2}(p) \frac{(ER_B(p)+V_{M,2}Z_r(p))(R_4+R_A(p))+R_{int}[V_{M,2}(R_A(p)+R_4+Z_r(p))+V_{M,1}R_B(p)]}{(Z_r(p)+R_B(p))(R_4+R_A(p))+R_{int}(Z_r(p)+R_4+R_A(p)+R_B(p))} \quad (25)$$

$$\text{with } R_A(p) = \frac{R_3 Z_{S,1}(p)}{R_3 + Z_{S,1}(p)}; R_B(p) = \frac{R_2 Z_{S,2}(p)}{R_2 + Z_{S,2}(p)} \text{ and } A'_{d,i}(p) = \frac{1}{A_{d,i}^{1\text{kHz}}} \frac{Z_{osc}(p)}{Z_{S,i}(p)} \text{ (} Z_{osc}(p) \text{ and } Z_{S,i}(p)$$

are detailed in eq. (17) for the direct connections to the oscilloscope method and eq. (18) for passive probes measurements). $A_{d,i}^{1\text{kHz}}$ is the compensated attenuation factor of the TPP1000 passive probe defined at the 1 kHz frequency of the probe compensation procedure square wave (see compensation procedure associated to eq. (19) and eq. (20)). In the case of direct connections to the oscilloscope, the voltage divider attenuation $Z_{osc}(p)/Z_{S,i}(p)$ is not compensated, thus $A_{d,i}^{1\text{kHz}} = 1$.

With the assumption that passive probes or direct connection cables are well matched ($Z_{S,1}(p) \approx Z_{S,2}(p) \approx Z_S(p)$) as well as ground leads voltages ($V_{M,1} \approx V_{M,2} \approx 0V$), the expression of eq. (25) can be simplified as follows:

$$V_{output}(p) = A'_d(p) \mathfrak{A}_{AB}(p) \quad (26)$$

$$\text{with } \mathfrak{A}_{AB}(p) \text{ described by eq. (14) in section 4.1 and } A'_d(p) = \frac{1}{A_d^{1\text{kHz}}} \frac{Z_{osc}(p)}{Z_S(p)} \text{ (} Z_{osc}(p) \text{ and } Z_S(p)$$

are still detailed in eq. (17) for the direct connections to the oscilloscope method and eq. (18) for passive probes measurements).

A numerical inversion of Laplace transforms using the De Hoog algorithm [37] applied to eq. (23) for the TDP3500 differential probe and to eq. (26) for pseudo-differential measurements gives the measured voltage $V_{output}(t)$. Figure 32 and Figure 33 show, respectively for $R_p = 10 \Omega$ and $R_p = 100 \Omega$, the distortions of the electrothermal signal according to the measuring device for a glass sample. Results on an AlN sample (material with the highest dynamic response, see Figure 16 in section 3.3) are displayed in the same conditions in Figure 34 and Figure 35. In each case, a comparison with a TDP3500 differential probe signal fully rejecting the common mode voltage (“perfect CMRR”) is provided ($\mathfrak{Q}_{cm}(p)/CMRR(p) = 0$ in eq. (23)). It is reminded that a cable impedance $Z_{cable}(p) = 50 \Omega$ is considered for the oscilloscope used on its own measurement case.

A bilayer model “ T_m^{si} ” (eq. (9) in section 3.3) is used for these simulations. The signal without distortions refers to the differential voltage $\mathfrak{Q}_{AB}(p)$ (see eq. (11)) with $Z_s(p)$ as an infinite impedance (no probe loading effects).

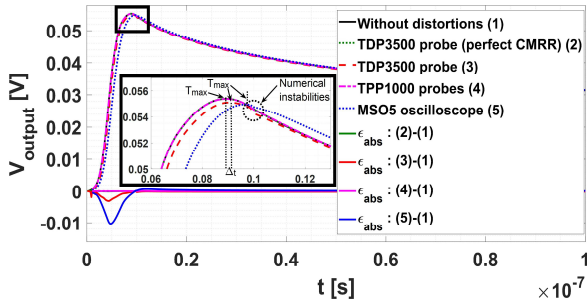


Figure 32. V_{output} measured by various devices, for a glass sample (Sample n°1). $R_p = 10 \Omega$, “ T_m^{si} ” model, $E = 6 V$. Insert: zoom on maximal voltage

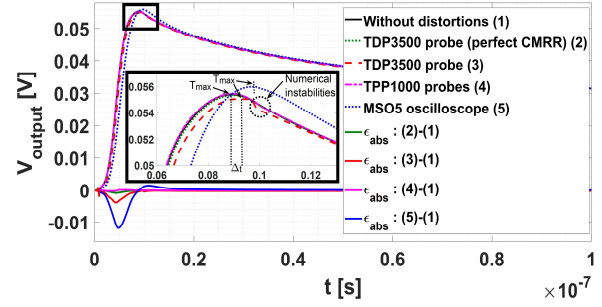


Figure 33. V_{output} measured by various devices, for a glass sample (Sample n°1). $R_p = 100 \Omega$, “ T_m^{si} ” model, $E = 6 V$. Insert: zoom on maximal voltage

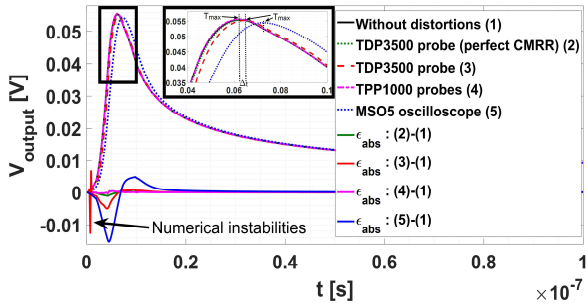


Figure 34. V_{output} measured by various devices, for an AlN sample (Sample n°2). $R_p = 10 \Omega$, “ T_m^{si} ” model, $E = 6 V$. Insert: zoom on maximal voltage

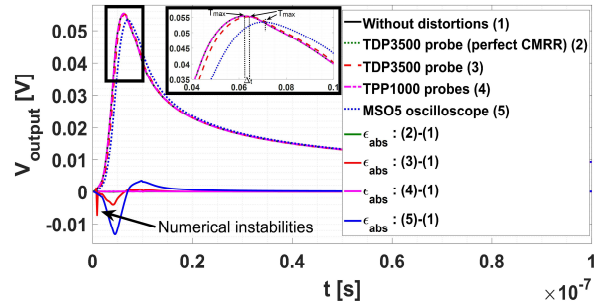


Figure 35. V_{output} measured by various devices, for an AlN sample (Sample n°2). $R_p = 100 \Omega$, “ T_m^{si} ” model, $E = 6 V$. Insert: zoom on maximal voltage

Table 5 summarizes the maximum relative errors $|\epsilon_{rel,max}| = \max \left(\left| \frac{\epsilon_{abs}(t)}{\max(V_{output,(1)}(t))} \right| \right)$

obtained by comparing each signal affected by a measuring device with the signal without distortions, where $\max(V_{output,1}(t))$ is the maximum voltage value of the undistorted signal and $\epsilon_{abs}(t)$ the difference between this signal and the signal affected by the device.

Use of higher bridge resistors values contributes to a more distorted signal (R_p/Z_s ratio, illustrated in Figure 25, is higher), especially when the signal dynamic is important (case of the AIN sample). This leads to a preference for low resistors values, as shown in the bridge sensitivity study (Figure 22). Limits discussed on this occasion are still valid though (electrical and thermal ones).

Measurements realized with the TDP3500 differential probe show more discrepancies with the signal without distortions than passive probes pseudo-differential measurements. It is mostly due to the additional consideration of the common mode rejection (modelling of this effect for the TDP3500 probe is addressed in section 4.2.2 while the impact of its non-ideality is highlighted in Table 5 with results obtained for a perfect rejection of this voltage). Still, pseudo-differential measurements realized with the oscilloscope used on its own - which also does not consider the common mode influence in this paper - show even more discrepancies, making it the measurement method providing the most distorted signal.

On the contrary, when neglecting this common mode additional voltage, 1 GHz passive probes appear to be adapted to the frequencies of the measured signals ($|\epsilon_{rel,max}| \leq 0.8\%$) and stand even more when compared to the oscilloscope used on its own ($|\epsilon_{rel,max}| \leq 28\%$). They also seem to provide a slightly less distorted signal than the differential probe signal with perfect CMRR ($|\epsilon_{rel,max}| \leq 2\%$), which is consistent with the observation in Figure 25 that the influence of the input impedance Z_s is slightly lower for pseudo-differential measurements. However, it will be shown experimentally that the measurements carried out with TPP1000 passive probes show more noise than TDP3500 differential probe measurements, but also that the differential probe setup is more robust when it comes to signal distortions through a better rejection of the common mode voltage and lower sensitivity to introduced transmission lines (by probes cables and ground leads, see section 5).

Finally, devices non-idealities alter the time of the maximum voltage and delay it (see inserts in Figure 32 to Figure 35) due to their equivalent input capacitance, along with its amplitude due to their equivalent input resistance. In the case of the oscilloscope used on its own, the improper attenuation factor is also influencing the measurements ($Z_{cable}(p) = 50\ \Omega$).

Nevertheless, all parasitic effects are reduced during the relaxation phase ($t > 20\ ns$); The signals end up overlapping, indicating weaker electrothermal distortions on this portion of the

signal, as predicted by the initial study in section 2 of the frequency spectra of the concerned materials. It leads to a preference for the relaxation phase of the signal for its exploitation.

	R_p [Ω]	Glass $\lambda_f = 1 \text{ W} \cdot \text{s}^{-1} \cdot \text{K}^{-1}$		AlN $\lambda_f = 92 \text{ W} \cdot \text{m}^{-1} \cdot \text{K}^{-1}$	
		complete	relaxation	complete	relaxation
Portion of signal:					
$ \epsilon_{rel,max} $ TDP 3500	10	5.6 %	0.6 %	13.0 %	1.3 %
	100	7.0 %	0.7 %	22.7 %	1.6 %
$ \epsilon_{rel,max} $ TDP 3500 (perfect CMRR)	10	0.2 %	0.0 %	0.2 %	0.0 %
	100	1.5 %	0.1 %	2.0 %	0.4 %
$ \epsilon_{rel,max} $ TPP 1000	10	0.3 %	0.1 %	0.2 %	0.2 %
	100	0.4 %	0.1 %	0.8 %	0.4 %
$ \epsilon_{rel,max} $ MSO5	10	18.6 %	1.7 %	23.8 %	7.9 %
	100	21.4 %	2.7 %	27.5 %	8.8 %

Table 5. Comparisons between the electrothermal models considering the measuring devices influence and the reference signal without distortions

In addition, effect of the probe cable modelling by a resistive impedance ($Z_{cable}(p) = 50 \Omega$, *i.e.* lossless cables with high bandwidth) is illustrated for the passive TPP1000 probes in Figure 36 on an AlN sample (for $R_p = 100 \Omega$). Additional distortions come from the cable impedance not compensated at high frequencies (see Figure 28), resulting in a different attenuation factor realized by the voltage divider for those frequencies. The impact of this effect, difficult to estimate due to the lack of precision in the consideration of the cable impedance in device datasheet, is reduced with respect to frequency, thus further encouraging to focus on the signal relaxation for its exploitation.

Also, the behaviour of cables modelled as transmission lines (coaxial cables, see Figure 29 and eq. (17) where $Z_{osc}(p)$ is defined in eq. (21) and $Z_{cable}(p)$ in eq. (22)) is illustrated in Figure 37 in the case of the oscilloscope used on its own.

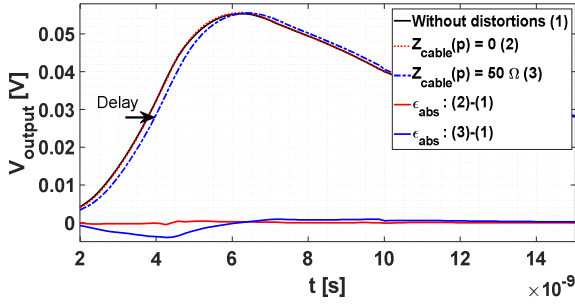


Figure 36. Impact of a resistive cable impedance on the signal measured with passive TPP1000 probes (AIN – Sample n°2, $R_p = 100 \Omega$, 4-slopes heat flux excitation)

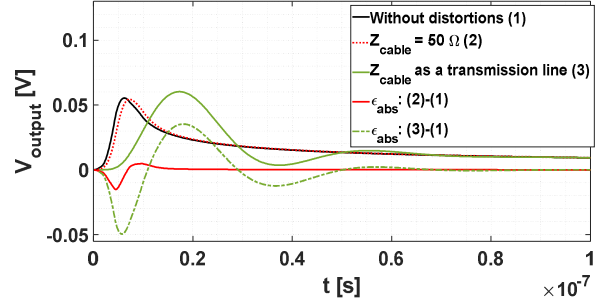


Figure 37. Impact on the signal considering transmission lines connections to the MSO5 oscilloscope (AIN - Sample n°2, $R_p = 100 \Omega$, 4-slopes heat flux excitation). The transmission lines modelling is available in Figure 29

A sinusoidal behaviour is exhibited and experimentally observed if no attention is paid to the connections and cable lengths used (for the bridge, power supply, ...) regardless of the measuring device (see experimental signal in Figure 38 measured with a TDP3500 differential probe on a glass sample). This problematic also affects the signal slope and the time of the signal maximum, as highlighted in Figure 39 for experimental measurements conducted with various length of cables connecting the transducer to the Wheatstone bridge (measurements performed with TPP1000 passive probes). It is particularly noticeable when comparing the black curve (maximum cables length) to the other two (with reduced cables lengths).

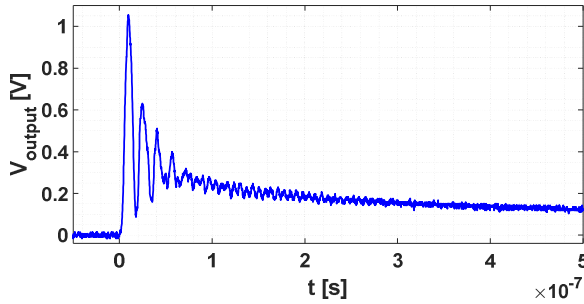


Figure 38. Experimental signal exhibiting a transmission line behaviour obtained with a TDP3500 differential probe on a 1 mm thick glass sample

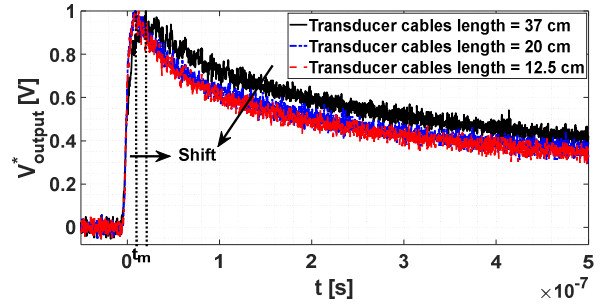


Figure 39. Experimental signals obtained with TPP1000 passive probes on a 1 mm thick glass sample for various length of the cables connecting the transducer to the Wheatstone bridge

4.2.2. Differential probe: modelling of the Common Mode Rejection Ratio

While it is difficult to quantify the contribution of the common mode for pseudo-differential measurements, the frequency-dependent rejection of the common mode voltage (CMRR) by a differential probe (see eq. (23) and eq. (24)) is usually provided by its manufacturer. Thus,

the typical CMRR available on the data sheet of the TDP3500 [43] was digitalized (see Figure 40, black curve) and modelled by a first-order low-pass filter such as:

$$CMRR(p) = \frac{K}{1 + \frac{1}{2\pi f_{c,1}} p} \quad (27)$$

where $K = 90$ and the cut-off frequency $f_{c,1}$ can be estimated by a least square method [35]. As the estimated curve shown in Figure 40 (blue curve) is “optimistic” in regard to the cut-off frequency ($f_{c,1} \approx 48 \text{ MHz}$), two other modelling, still using eq. (27) but with lower cut-off frequencies values, are compared and displayed in Figure 40: a “pessimistic” one ($f_{c,1} = 500 \text{ kHz}$, brown curve) and an “intermediary” one ($f_{c,1} = 5 \text{ MHz}$, red curve). Effects of these modelling on the TDP3500 probe output signal are compared in Figure 41 for an AlN sample. The influence of the imperfect differential probe CMRR at high frequencies is highlighted thanks to their comparison with a perfect CMRR signal ($\mathcal{U}_{cm}(p)/CMRR(p) = 0$ in eq. (23)).

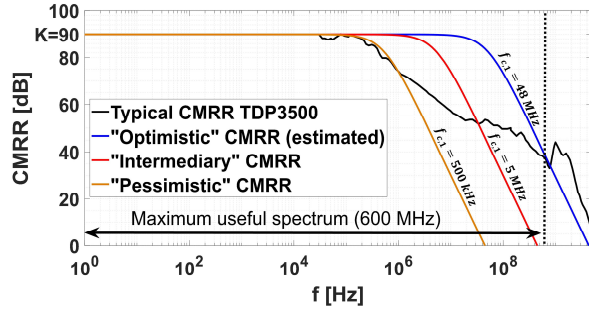


Figure 40. Modelling of the TDP3500 probe CMRR by first-order low-pass filters (cut-off frequency indicated)

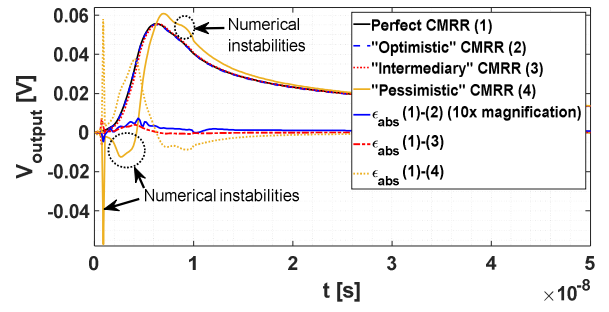


Figure 41. Imperfect CMRR influence on the TDP3500 probe output signal for 3 different CMRR modelling (Sample $n^{\circ}2$ – AlN, $R_p = 100 \Omega$, $E = 6V$, “ T_m^{si} ” model, 4-slopes heat flux)

Comparison of the residues confirms a greater degradation of the signal when the cut-off frequency of the CMRR modelling is lower. In the case of the “optimistic” modelling of the CMRR, the degradations are clearly insignificant. On the contrary, the signal is strongly distorted in the heating phase of the signal for a “pessimistic” CMRR modelling due to the higher frequency dynamic in this part (with further distortions visible at the beginning of the relaxation phase, see Figure 41). This CMRR modelling being drastic with respect to the cut-off frequency considered and exhibiting many numerical instabilities, the “intermediary” modelling of the probe CMRR is preferred and used for TDP3500 probe simulations in this paper (as in Figure 32 to Figure 35).

Furthermore, numerical instabilities presented in Figure 41 are greatly reduced when using a heat flux temporal shape modelling with fewer parameters, such as the triangle shape (see

eq. (4) in section 3.2). They can also be reduced by generating the signal from the relaxation phase, which is not a problem since it has been shown in section 4.2.1 that it is preferable to focus on this part of the signal to limit electrothermal distortions.

The reduction of numerical instabilities is illustrated for the AlN sample in Figure 42, under the same conditions as in Figure 41 while using a triangle shape (see eq. (4) in section 3.2) and t_0 as the time of the maximum voltage of the perfect CMRR model (experimentally, t_0 is to be chosen as the time of the experimental signal maximum voltage). The probe CMRR performances on a glass sample are also displayed in Figure 43, where common mode influence appears to be weaker due to the lower thermal dynamic of the glass sample (see section 2).

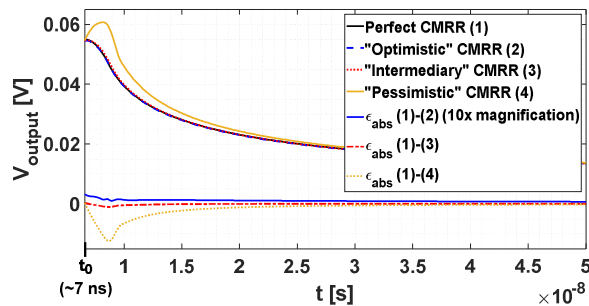


Figure 42. Imperfect CMRR influence on the TDP3500 probe output signal for three different CMRR modelling (Sample n°2 – AlN, $R_p = 100 \Omega$, $E = 6V$, “ T_m^{si} ” model, triangle heat flux, $t_0 \approx 7 \text{ ns}$)

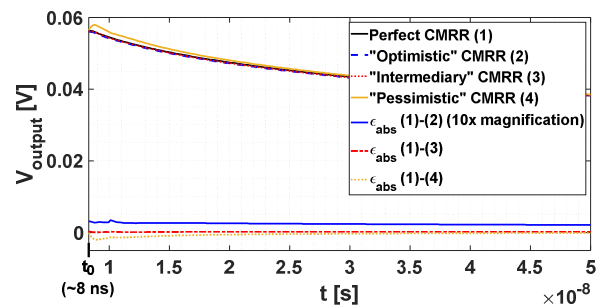


Figure 43. Imperfect CMRR influence on the TDP3500 probe output signal for three different CMRR modelling (Sample n°1 – Glass, $R_p = 100 \Omega$, $E = 6V$, “ T_m^{si} ” model, triangle heat flux, $t_0 \approx 8 \text{ ns}$)

First experimental tests conducted on glass samples, presented in section 5, will highlight a delay on the heating part of the experimental signal and tend to indicate that the TDP3500 CMRR behaviour is closer to the “intermediary” and “pessimistic” modelling.

A better modelling of the CMRR behaviour can be achieved, as shown in Figure 44, thanks to a 1-slope (blue curve, described by eq. (28)) and a 3-slopes (red curve, described by eq. (29)) fitting expressions expressed in the Laplace domain (estimated parameters are indicated in Figure 43). Unfortunately, strong numerical instabilities then appear on the computed V_{output} signal due to the numerical Laplace inversion, making the results unusable and restricting to the use of low-pass first order filter expressions for CMRR modelling.

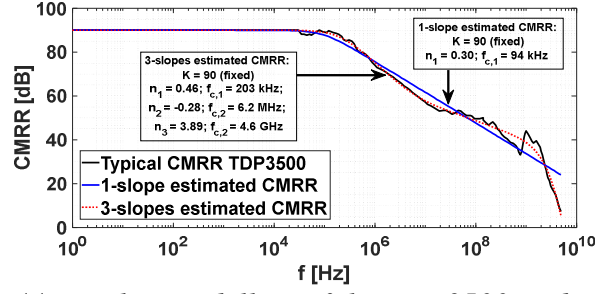


Figure 44. Further modelling of the TDP3500 probe CMRR

$$CMRR(p) = \frac{K}{\left(1 + \frac{1}{2\pi f_{c,1}} p\right)^{n_1}} \quad (28)$$

$$CMRR(p) = \frac{K}{\left(1 + \frac{1}{2\pi f_{c,1}} p\right)^{n_1}} \frac{1}{\left(1 + \frac{1}{2\pi f_{c,2}} p\right)^{n_2}} \frac{1}{\left(1 + \frac{1}{2\pi f_{c,3}} p\right)^{n_3}} \quad (29)$$

4.2.3. Modelling of the Analog-to-Digital Conversion

Finally, the measured analog signal is digitalized by the oscilloscope (Analog-to-Digital Conversion - ADC). The MSO5 oscilloscope offers two configurations to this end, either enhancing sampling (6.25 GS/s, 8 bits) or accuracy (3.125 GS/s, 12 bits, resulting in twice less measurement points) [49]. All presented electrothermal signals use the first configuration (displaying $nt = 6249$ points for a 1 μ s long study), without the quantification effects.

This last effect can be modelled. Indeed, to a voltage measure $V_{output}(t_i)$ such that:

$$k \cdot q - \frac{q}{2} \leq V_{output}(t_i) < k \cdot q + \frac{q}{2} \quad (30)$$

corresponds the closest of the two values (closest conversion law), with $\frac{q}{2} = \frac{V_{input,m}}{2(2^n - 1)}$ the quantification error, $V_{input,m}$ being the full scale (maximum) voltage that can be displayed on the oscilloscope channel, n the number of bits (8 bits or 12 bits for the MSO5 oscilloscope) and $k \in \{0; \dots; k_{max}\}$ such that $k_{max} \cdot q = V_{input,m}$.

An illustration of this quantification effect is given in Figure 45 for a TDP3500 differential probe signal (“intermediary” CMRR) and will be provided in the case of an experimental measurement (see section 5). Better accuracy is observed with the 3.125 GS/s, 12 bits configuration. Effect of this process while reducing the number of measurements points for the estimation parameter will be investigated in a subsequent study.

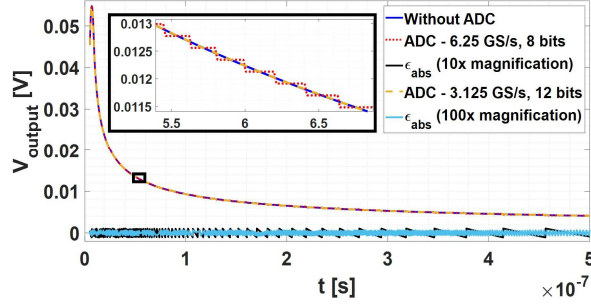


Figure 45. Illustration of the oscilloscope MSO5 ADC effect on a TDP3500 differential probe signal (Sample $n^{\circ}2$ – AlN, $R_p = 100 \Omega$, $E = 6V$, “ T_m^{si} ” model, 4-slopes heat flux, $t_0 = 5$ ns). Insert: zoom

5. First experimental results on glass samples

First experiments were conducted with the setup described in section 2 to assess whether exploitable signals could be obtained. Tests were conducted on a $e_f = 1$ mm thick glass sample on which a $e_r = 200$ nm thick aluminium serpentine transducer (presented in Figure 2 (b) - left sample) was deposited by Joule effect evaporation. The Wheatstone bridge was balanced accordingly to the $\sim 20 \Omega$ resistance of the transducer and supplied with a $E = 6$ V voltage, resulting in the two signals proposed in Figure 46 after laser excitation. The differential voltage of the bridge was measured either by using a TDP3500 differential probe (differential probe method, described in Figure 20 (a), section 4.1) or two TPP1000 passive probes (pseudo-differential method with two passive probes, as shown in Figure 20 (b), section 4.1).

Signals appear to be similar, though with a higher level of noise for the two passive probes measurements. However, Figure 47 highlights a delay on the rise time of the pseudo-differential signal compared to the differential probe one, along with an amplitude shift. This behaviour seems similar to the common mode effect modelled in section 4.2.2 for the TDP3500 probe (see Figure 41 and Figure 43 in the mentioned section) which could hardly be considered for pseudo-differential measurements. It can be caused by the influence of the ground leads cables inductances, their positioning on the circuit (resulting in a potential voltage difference of each probe ground references – see eq. (13) by posing $V_{M,1}(p) \neq V_{M,2}(p)$), or the non-ideal symmetry of the two passive probes ($Z_{s,1}(p) \neq Z_{s,2}(p)$ in eq. (13)). It highlights, at least, a better reliability of the differential probe set-up, leading to a preference for the latter. It is however pointed out that both signals eventually overlap for $t \geq 20$ ns (indicated in Figure 47 and clearly visible in Figure 46); the distortions caused by the acquisition chain are reduced later after the signal rise (see Figure 32 to Figure 35 in section

4.2) due to smaller frequency spectrum range (see section 2).

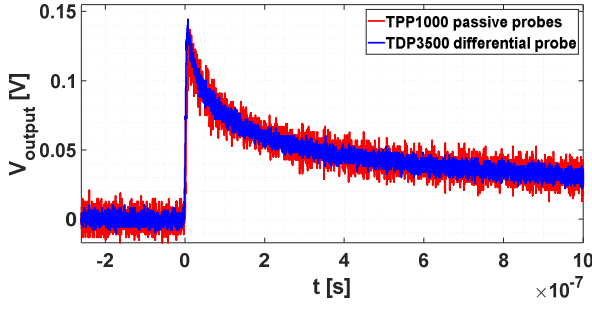


Figure 46. Experimental results obtained with a pseudo-differential (TPP1000 probes) and differential probe (TDP3500 probe) measurements methods on a 1 mm thick glass sample (ADC = 6.25 GS/s, 8 bits)

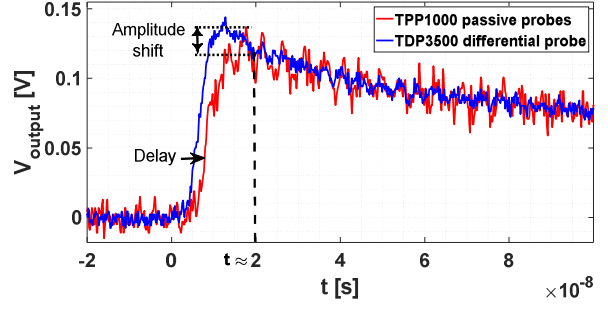


Figure 47. Evidence of experimental non-idealities of the pseudo-differential method with passive probes (zoom on the signal rise of Figure 46)

An illustration of the sampling and quantification procedure (ADC) of the experimental noisy signal (see section 4.2) is provided in Figure 48 for two measurements with the differential probe, in another experimental condition (laser deposited energy and new sample of same characteristics). Slightly less noise is observed while prioritizing accuracy (3.125 GS/s, 12 bits) over sampling (6.25 GS/s, 8 bits). Effect on the characterization procedure will have to be investigated.

Direct electrothermal models developed in sections 3 and 4 are applied to the differential probe signal displayed in Figure 46 through a very simplified parameter estimation procedure for a first illustrative test. To reduce the number of uncertain parameters, a thermal diffusion in a capacitive aluminium transducer on a semi-infinite glass sample is considered (" T_c^{si} " model, see section 3.3 and eq. (10)). In comparison to a mean temperature transducer modelling (" T_m^{si} " model, see section 3.3 and eq. (9)), the use of this model allows to get rid of the knowledge or estimation of the transducer conductivity λ_r . This modelling is possible in first approximation thanks to the small maximum relative error observed between these two models in section 3.3 for a glass sample ($\epsilon_{rel,max} \approx 2\%$, however its validity will be further investigated in subsequent studies). This bias is reduced by focusing on the relaxation phase of the signal $[t_m; t_{end}]$ for the estimation process (reducing the maximum relative error to $\epsilon_{rel,max} \approx 0.5\%$), where the initial time t_m is defined as the time of the experimental signal maximum while the end time t_{end} is limited to $1\ \mu\text{s}$ (1D heat transfer condition and semi-infinite sample). The signal is then reconstructed on the full-time of the experiment (*i.e.* heating/rise and relaxation phases).

Furthermore, properties of the transducer are assumed to be known (using values indicated in Table 1 in section 2), with the exception of the reflectivity of the transducer - and therefore

the heat flux absorbed φ_m (see eq. (7) in section 3.2 while considering a 4-slopes heat flux time shape described in eq. (6)) - and its thermal coefficient α_r . The $\alpha_r \varphi_m$ coefficient (see eq. (1)) is thus estimated along with the sample (glass) conductivity λ_f by using a least square method associated with a regularized Levenberg-Marquardt descent algorithm [35].

This algorithm minimizes the sum of the quadratic deviations between the experimentally measured differential voltage $\Delta V_{output,exp}$ and the computed voltage ΔV_{calc} . The latter either takes into consideration the thermal diffusion of the sample (“ T_c^{si} ” model” with due amplitude adaptation) only, or with additional electrothermal distortions caused by the TDP3500 differential probe (see eq. (23), for the three modelling of the probe’s CMRR – “optimistic”, “intermediary” and “pessimistic” - described in section 4.2). It results in the minimization of the following cost function:

$$J(\boldsymbol{\beta}) = \sum_{k=k_1}^{k_2} \left(\Delta V_{output,exp}(t_k) - \Delta V_{calc}(t_k, \boldsymbol{\beta}) \right)^2 \Rightarrow \hat{\boldsymbol{\beta}} = \arg \min_{t \in [t_m; t_{end}]} (J(\boldsymbol{\beta})) \quad (31)$$

where $\boldsymbol{\beta} = (\lambda_f; kE\alpha_r\varphi_m)$ is the parameter vector to be estimated with k a coefficient. Note that a proper sensibility analysis to parameters will be realized in a subsequent study focused on the estimation procedure.

Results are displayed in Figure 49 on the full-time of the experiment while only considering the thermal diffusion in the sample. The estimated conductivity $\lambda_{f,estimated}$ is indicated in Table 6 and found within a 10 % range of the theoretical glass conductivity of $1 \text{ W} \cdot \text{m}^{-1} \cdot \text{K}^{-1}$ such as $0.9 \text{ W} \cdot \text{m}^{-1} \cdot \text{K}^{-1} < \lambda_{f,estimated} < 1.1 \text{ W} \cdot \text{m}^{-1} \cdot \text{K}^{-1}$.

Comparison with electrothermal modelling is displayed in Figure 50 on the rise time of the signal where electrothermal distortions appear (see section 4.2.1). Estimated conductivity values are indicated in Table 6.

Estimation results obtained while considering a triangle heat flux (see eq. (5) in section 3.2) are also displayed in Figure 51 and indicated in Table 6.

Estimation model	$\lambda_{f,estimated}$ [$\text{W} \cdot \text{m}^{-1} \cdot \text{K}^{-1}$]		\bar{m} [V]		σ [V]
	4-slopes	triangle	4-slopes	triangle	4-slopes and triangle
" T_c^{si} "	1.06	1.07	$7 \cdot 10^{-5}$	$3 \cdot 10^{-5}$	$3.5 \cdot 10^{-3}$
TDP3500 ("optimistic" CMRR)	1.06	1.07	$6 \cdot 10^{-5}$	$3 \cdot 10^{-5}$	
TDP3500 ("intermediary" CMRR)	1.05	1.06	$5 \cdot 10^{-5}$	$4 \cdot 10^{-5}$	

TDP3500 ("pessimistic" CMRR)	1.00	1.01	$4 \cdot 10^{-5}$	$2 \cdot 10^{-5}$	
------------------------------------	------	------	-------------------	-------------------	--

Table 6. Estimated conductivities $\lambda_{f,estimated}$ on the experimental signal measured by the TDP3500 differential probe. The residuals mean value \bar{m} and the standard deviation σ on $[t_m; t_{end}]$ are indicated ($\bar{m} = \frac{1}{nt} \sum (\Delta V_{output,exp} - \Delta V_{calc})$ [V] and $\sigma = \sqrt{Var(\bar{m})}$ [V]). Results are associated with visuals in Figure 49 and Figure 50 for 4-slopes heat flux, and in Figure 51 for triangle heat flux

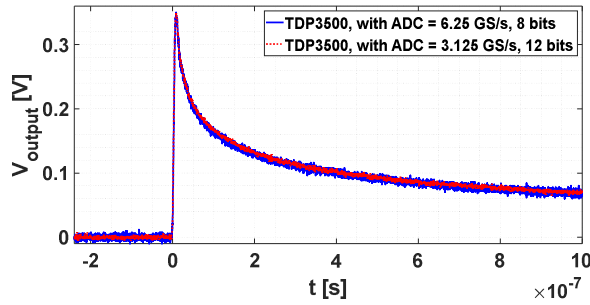


Figure 48. Visual illustration of ADC influence on the TDP3500 differential probe measurements

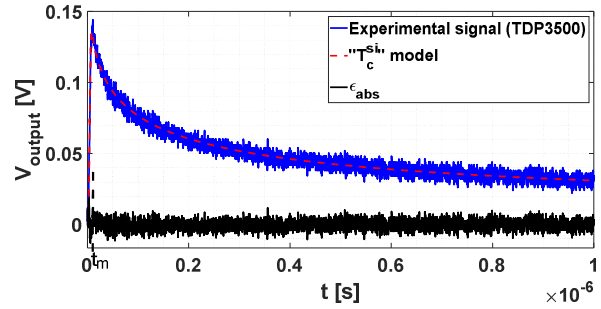


Figure 49. Estimated signal on $[t_m; t_{end}]$, reconstructed on the full-time of the experiment (with $\lambda_{f,estimated} = 1.06 \text{ W} \cdot \text{m}^{-1} \cdot \text{K}^{-1}$, 4-slopes heat flux)

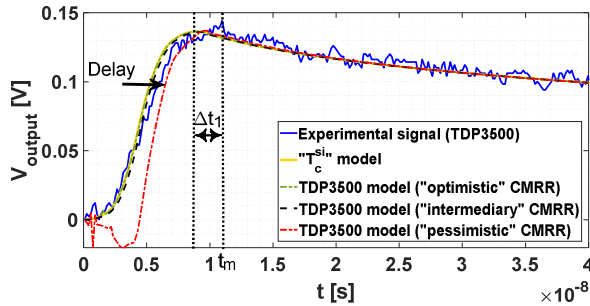


Figure 50. Estimated signals reconstructed on the full-time of the experiment, with electrothermal models considering the TDP3500 differential probe influence and three modelling of its CMRR (zoom on the heating phase). Estimated values of $\lambda_{f,estimated}$ are indicated in Table 6 (4-slopes heat flux)

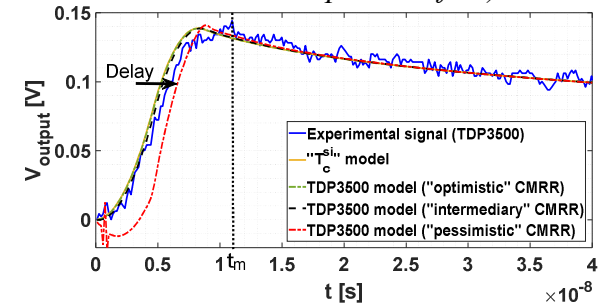


Figure 51. Estimated signals reconstructed on the full-time of the experiment, with electrothermal models considering the TDP3500 differential probe influence and three modelling of its CMRR (zoom on the heating phase). Estimated values of $\lambda_{f,estimated}$ are indicated in Table 6 (triangle heat flux)

A good agreement is observed at first sight in Figure 49 between the experimental signal and the thermal modelling. It is highlighted by the low and zero mean value ($\sim 7 \cdot 10^{-5} \text{ V}$ with a standard deviation of $3 \cdot 10^{-3} \text{ V}$) of the residuals on the estimation time of the signal ($[t_m; t_{end}]$) and tend to validate the modelling of the bench behaviour. However, Figure 50 highlights that the time of the experimental maximum and that of the thermal model signal

show a small difference ($\Delta t_1 \approx 2.2 \text{ ns}$). This can be explained by an error in the heat flux modelling (see Figure 5 - it is also reminded that a new photodiode is needed for subsequent parameter estimation due to distortions on the laser collected signal mentioned in section 3.2) and/or the definition of the experimental signal initial time (measure triggering) as well as the cables' contribution (see Figure 39 in section 4.2.1). The estimation was performed on the relaxation phase of the signal to reduce their impacts.

Another possibility is the influence of the differential probe on the measurements. Indeed, the models considering the probe and its Common Mode Rejection Ratio (CMRR) tend to be closer to the experimental maximum: if the “pessimistic” modelling presents strong discrepancies at the beginning of the heating phase (phase of the signal with the largest frequency range – see Table 3 - *i.e.* the frequency range of the probe typical CMRR which is not modelled accurately by the pessimistic modelling due to its low cut-off frequency, see the brown curve in Figure 40), it is more accurate around the signal maximum (times of the signal maximum delayed by $\Delta t \approx 1.3 \text{ ns}$ - even less if the experimental maximum at the time t_m is considered as a noisy point). The performances of the TDP3500 probe would therefore be between the “pessimistic” and “intermediary” models for the glass sample frequency range. Therefore, these models seem to provide a good approximation of the electrothermal behaviour of the bench while using a TDP3500 differential probe.

Furthermore, the estimation results obtained with a triangle heat flux modelling show little difference with those achieved with the 4-slopes excitation (no more than $\sim 1 \%$ of difference in the estimation in regard with glass theoretical conductivity, see Table 6). Heat flux modelling (and numerical instabilities with the CMRR modelling, see section 4.2.2) thus shows little influence by performing the estimation on the relaxation phase of the signal.

It is reminded that the applications proposed here are for illustrative purposes only. The validation of the bench will be done through the proper estimation of an effective thermal conductivity (or diffusivity) once an inverse method has been implemented in a future work. It will then be possible to characterize the performances of the bench on various materials, over a wide range of conductivities and conduction times.

6. Conclusions

This paper introduced the design and characteristics of an opto-electrothermal bench (front-face laser excitation combined with an electrothermal measurement) aiming for the thermal characterization of materials over a wide range of conduction times (from seconds to a few tens of nanoseconds). It has the potential to cover both low thermal conductivity samples

(like polyethylene, $\sim 0.5 \text{ W}\cdot\text{m}^{-1}\cdot\text{K}^{-1}$, and glass, $1 \text{ W}\cdot\text{m}^{-1}\cdot\text{K}^{-1}$) and high conductivity materials such as AlN ($100 \text{ W}\cdot\text{m}^{-1}\cdot\text{K}^{-1}$ and more). Here, first results on glass and AlN samples were investigated.

In this perspective, a methodology applicable to other electrothermal measurement methods for designing an acquisition chain adapted to the frequency spectrum of such materials was presented. The combination of a Wheatstone bridge coupled to the frequency response of various measuring devices (differential probe, passive measuring probes or oscilloscope used on its own) was modelled. As a result, first electrothermal models were developed, considering the thermal behaviour of a multilayer sample and the distortions depending on the frequency response of the acquisition chain to the sample's thermal dynamics.

Furthermore, a sensitivity study has shown that an optimum of the bridge is found when the four resistors constituting it are of the same value. However, the higher these resistors are, the more sensitive the acquisition chain is to the imperfections of the used measuring device (bridge resistor to measuring device impedance ratio R_p/Z_s should be inferior to 10^{-1} to reach at least 90 % of the sensitivity of a Wheatstone bridge without source loading effects induced by the measuring device). The latter is therefore likely to degrade the estimation of parameters, even more so with the common mode voltage which has been considered here by modelling the frequency dependent common mode rejection ratio of a differential probe. Particular attention must therefore be paid to all measurements, especially if equipment not suitable for high frequency measurements (600 MHz) is used.

Indeed, first experimental measurements conducted on a glass sample with a high-frequency differential probe (3.5 GHz) and two high-frequency passive probes (1 GHz) revealed the presence of a time delay and a reduced amplitude of the signal rise (heating) measurements when using the passive probes. The use of a - correctly sized – differential probe, whose performances and reliability seem to be better at high frequencies, is therefore preferred.

However, both signals eventually overlap, as modelling has shown that the relaxation (cooling) phase of the signal is less sensitive to disturbances from the acquisition chain. This is consistent with the evidence that, thanks to a Discrete Cosine Transform, the high frequency spectral content is mainly carried on the heating phase (a maximum frequency is found of 600 MHz for an AlN sample and reduced to 300 MHz when restricted to the cooling phase).

Furthermore, while thermal modelling will be the subject of future works, initial checks of the 1D thermal diffusion nature in the sample have been carried out by assessing the flatness of the laser excitation. Different modelling of the temporal shape of the laser heat flux have been proposed, including a 4-slopes expression in the Laplace domain that has shown in first

approximation a good agreement with the experimentally collected heat flux time shape. These models, along with the electrothermal ones developed in this paper and further advanced thermal models to come, permit elaborating a digital twin of the electrothermal bench. They will serve as a basis for future work consisting in the implementation of an inverse method for the estimation of an effective thermal conductivity (or diffusivity). They will be used as both the simulation and the inverse models, and will further allow the study in a simplified framework of the effects of biases caused by the acquisition chain on the parameter estimation. The validation of the experimental bench will then be possible once the estimation procedure is set, which will also permit the study of its real performances on various materials over a wide range of conductivities.

Involvement

This work has been co-supported by Région Occitanie and EPF Ecole d'Ingénieur-e-s. Authors have been cited in the order of their involvement. The writing and scientific content were realized by PEILLON Sébastien and RODIET Christophe. The transducer deposition on glass samples was funded thanks to NOTINGHER Petru and performed by FÉLIX Renaud. Bench equipment costs were covered by EPF Ecole d'Ingénieur-e-s.

References

- [1] W. J. Parker, R. J. Jenkins, C. P. Butler, and G. L. Abbott, 'Flash Method of Determining Thermal Diffusivity, Heat Capacity, and Thermal Conductivity', *Journal of Applied Physics*, vol. 32, no. 9, pp. 1679–1684, Sep. 1961, doi: 10.1063/1.1728417.
- [2] K.-H. Lim, S.-K. Kim, and M.-K. Chung, 'Improvement of the thermal diffusivity measurement of thin samples by the flash method', *Thermochimica Acta*, vol. 494, no. 1–2, pp. 71–79, Oct. 2009, doi: 10.1016/j.tca.2009.04.019.
- [3] A. Cai, L. Yang, J. Chen, T. Xi, S. Xin, and W. Wu, 'Thermal Conductivity of Anodic Alumina Film at (220 to 480) K by Laser Flash Technique', *J. Chem. Eng. Data*, vol. 55, no. 11, pp. 4840–4843, Nov. 2010, doi: 10.1021/je100437j.
- [4] L. Vozár and W. Hohenauer, 'Flash method of measuring the thermal diffusivity. A review', *High Temp.-High Press.*, vol. 35/36, no. 3, pp. 253–264, 2003, doi: 10.1068/htjr119.
- [5] D. Zhao, X. Qian, X. Gu, S. A. Jajja, and R. Yang, 'Measurement Techniques for Thermal Conductivity and Interfacial Thermal Conductance of Bulk and Thin Film Materials', *Journal of Electronic Packaging*, vol. 138, no. 4, p. 040802, Dec. 2016, doi: 10.1115/1.4034605.

- [6] Y. Xian, P. Zhang, S. Zhai, P. Yuan, and D. Yang, ‘Experimental characterization methods for thermal contact resistance: A review’, *Applied Thermal Engineering*, vol. 130, pp. 1530–1548, Feb. 2018, doi: 10.1016/j.applthermaleng.2017.10.163.
- [7] A. Salazar, A. Mendioroz, E. Apiñaniz, C. Pradere, F. Noël, and J.-C. Batsale, ‘Extending the flash method to measure the thermal diffusivity of semitransparent solids’, *Meas. Sci. Technol.*, vol. 25, no. 3, p. 035604, Mar. 2014, doi: 10.1088/0957-0233/25/3/035604.
- [8] D. G. Cahill, ‘Thermal conductivity measurement from 30 to 750 K: the 3ω method’, *Review of Scientific Instruments*, vol. 61, no. 2, pp. 802–808, Feb. 1990, doi: 10.1063/1.1141498.
- [9] A. Moridi *et al.*, ‘Characterisation of high thermal conductivity thin-film substrate systems and their interface thermal resistance’, *Surface and Coatings Technology*, vol. 334, pp. 233–242, Jan. 2018, doi: 10.1016/j.surfcoat.2017.11.021.
- [10] A. J. Schmidt, R. Cheaito, and M. Chiesa, ‘A frequency-domain thermoreflectance method for the characterization of thermal properties’, *Review of Scientific Instruments*, vol. 80, no. 9, p. 094901, Sep. 2009, doi: 10.1063/1.3212673.
- [11] H. J. Kim, J. H. Kim, P. S. Jeon, and J. Yoo, ‘The measurement of thermal conductivities using the photothermal deflection method for thin films with varying thickness’, *J Mech Sci Technol*, vol. 23, no. 9, pp. 2514–2520, Sep. 2009, doi: 10.1007/s12206-009-0701-0.
- [12] B. Abad, D.-A. Borca-Tasciuc, and M. S. Martin-Gonzalez, ‘Non-contact methods for thermal properties measurement’, *Renewable and Sustainable Energy Reviews*, vol. 76, pp. 1348–1370, Sep. 2017, doi: 10.1016/j.rser.2017.03.027.
- [13] S. Orain, Y. Scudeller, S. Garcia, and T. Brousse, ‘Use of genetic algorithms for the simultaneous estimation of thin films thermal conductivity and contact resistances’, *International Journal of Heat and Mass Transfer*, p. 12, 2001.
- [14] C. Rodiet, M. Ramal, B. Rousseau, B. Garnier, and A. Djouadi, ‘Caractérisation thermique de couches minces par technique électrothermique : Validation numérique’, *SFT, Société Française de Thermique*, 2016.
- [15] C. Rodiet, Y. Cuminal, and A. Foucaran, ‘Développement et optimisation d’une méthode de caractérisation thermique de couches minces par technique électrothermique sur données synthétiques’, *SFT, Société Française de Thermique*, 2017.
- [16] M. Rammal *et al.*, ‘High Thermal Conductivity Thin Film for Heat Spreading Enhancement in Microelectronic Measured Using Short Pulsed Photothermal Technique’, in *International Heat Transfer Conference 16*, Beijing, China, 2018, pp.

7099–7106. doi: 10.1615/IHTC16.nmt.024428.

- [17] L. H. Sperling, *Introduction to physical polymer science*, 4th ed. Hoboken, N.J: Wiley, 2006.
- [18] G. Kalaprasad, P. Pradeep, G. Mathew, C. Pavithran, and S. Thomas, ‘Thermal conductivity and thermal diffusivity analyses of low-density polyethylene composites reinforced with sisal, glass and intimately mixed sisal/glass fibres’, *Composites Science and Technology*, p. 11, 2000.
- [19] X. Li, L. G. Tabil, I. N. Oguocha, and S. Panigrahi, ‘Thermal diffusivity, thermal conductivity, and specific heat of flax fiber–HDPE biocomposites at processing temperatures’, *Composites Science and Technology*, vol. 68, no. 7–8, pp. 1753–1758, Jun. 2008, doi: 10.1016/j.compscitech.2008.02.016.
- [20] GoodFellow, ‘Nitride d’Aluminium (BNP-2), Reference 699-127-15’. Accessed: Aug. 01, 2021. [Online]. Available: <http://www.goodfellow.com/>
- [21] A. Jacquot *et al.*, ‘Optical and thermal characterization of AlN thin films deposited by pulsed laser deposition’, *Applied Surface Science*, vol. 186, no. 1, pp. 507–512, 2002.
- [22] S. R. Choi, D. Kim, S.-H. Choa, S.-H. Lee, and J.-K. Kim, ‘Thermal Conductivity of AlN and SiC Thin Films’, *Int J Thermophys*, vol. 27, no. 3, pp. 896–905, Sep. 2006, doi: 10.1007/s10765-006-0062-1.
- [23] D. Sakami, A. Lahmar, Y. Scudeller, F. Danes, and J. P. Bardon, ‘Thermal contact resistance and adhesion studies on thin copper films on alumina substrates’, *Journal of Adhesion Science and Technology*, vol. 15, no. 12, pp. 1403–1416, Jan. 2001, doi: 10.1163/156856101753213268.
- [24] A. Jain and A. J. H. McGaughey, ‘Supplementary Information - Thermal transport by phonons and electrons in aluminum, silver, and gold from first principles’.
- [25] D. Gall, ‘Electron mean free path in elemental metals’, *Journal of Applied Physics*, vol. 119, no. 8, p. 085101, Feb. 2016, doi: 10.1063/1.4942216.
- [26] Quantel, ‘Q-smart (850 mJ), Nd:YAG’. Accessed: Aug. 01, 2021. [Online]. Available: https://www.quantel-laser.com/fr/produits/item/Q-SMART-850mj_fr.html
- [27] A. I. Oliva and J. M. Lugo, ‘The physical properties of nanomaterials: A challenge in materials science’, presented at the 2015 12th International Conference on Electrical Engineering, Computing Science and Automatic Control (CCE), Mexico City, Mexico, Oct. 2015. doi: 10.1109/ICEEE.2015.7357902.
- [28] Newport, ‘818-BB-35F Fiber-Optic Detector, 1000-1650 nm Battery Biased InGaAs Detector, 15 GHz, FC/UPC’. Accessed: Aug. 01, 2021. [Online]. Available: <https://www.newport.com/p/818-BB-35F>

- [29] Tektronix, ‘How Oscilloscope Probes Affect Your Measurement’. Accessed: Aug. 01, 2021. [Online]. Available: https://download.tek.com/document/51W_30013_0_MR_Letter.pdf
- [30] LeCroy Corporation, ‘Why Differential?’ Accessed: Aug. 01, 2021. [Online]. Available: http://cdn.teledynelecroy.com/files/whitepapers/wp_differential_measurements.pdf
- [31] Tektronix, ‘Probing Techniques for Accurate Voltage Measurements on Power Converters with Oscilloscopes’. Accessed: Aug. 01, 2021. [Online]. Available: https://download.tek.com/document/Voltage%20on%20Power%20Supplies_App-Note_51W-60161-3.pdf
- [32] Caddock Electronic, Inc., ‘MP900 and MP9000 series Kool-Pak’. Accessed: Aug. 01, 2021. [Online]. Available: http://www.caddock.com/Online_catalog/Mrktg_Lit/MP9000_Series.pdf
- [33] Newport, ‘818-BB-35 High Speed Photodetector, 1000-1650 nm Battery Biased InGaAs Detector, 15 GHz’. Accessed: Nov. 12, 2021. [Online]. Available: <https://www.newport.com/p/818-BB-35>
- [34] EOT, Electro-Optics Technology, Inc., ‘ET-3600 - 22 GHz InGaAs Photodetector’. Accessed: Nov. 12, 2021. [Online]. Available: <https://www.eotech.com/cart/117/photodetectors/%3E10-ghz-photodetectors/et-3600---22-ghz-ingaas-photodetector>
- [35] P. E. Gill and W. Murray, ‘Algorithms for the Solution of the Nonlinear Least-Squares Problem’, *SIAM Journal on Numerical Analysis*, pp. 977–992, 1978.
- [36] M. Tearle, *Simple real Fourier series approximation*. Accessed: Jul. 01, 2021. [Online]. Available: <https://www.mathworks.com/matlabcentral/fileexchange/31013-simple-real-fourier-series-approximation>
- [37] F. R. de Hoog, J. H. Knight, and A. N. Stokes, ‘An Improved Method for Numerical Inversion of Laplace Transforms’, *SIAM J. Sci. and Stat. Comput.*, vol. 3, no. 3, pp. 357–366, Sep. 1982, doi: 10.1137/0903022.
- [38] J.-L. Battaglia *et al.*, ‘The periodic pulse photothermal radiometry technique within the front face configuration’, *Measurement*, vol. 158, p. 107691, Jul. 2020, doi: 10.1016/j.measurement.2020.107691.
- [39] D. Maillet, *Thermal quadrupoles: solving the heat equation through integral transforms*, Wiley. Chichester ; New York, 2000.
- [40] A. Pini, ‘Understanding, Selecting, and Effectively Using Active Oscilloscope Probes’, Jul. 21, 2017. Accessed: Aug. 01, 2021. [Online]. Available: <https://www.digikey.fr/fr/articles/understanding-selecting-using-active-oscilloscope->

probes

- [41] LeCroy Corporation, 'Probing Tutorial'. Accessed: Aug. 01, 2021. [Online]. Available: http://cdn.teledynelecroy.com/files/appnotes/lecroy_probing_tutorial_appnote016.pdf
- [42] D. Ford, 'The Secret World Of Oscilloscope Probes', *Silicon Chip*, Oct. 2009. Accessed: Aug. 01, 2021. [Online]. Available: <http://www.dfad.com.au/links/THE%20SECRET%20WORLD%20OF%20PROBES%20OOCt09.pdf>
- [43] Tektronix, 'TDP3500 Differential probe'. Accessed: Aug. 01, 2021. [Online]. Available: <https://fr.tek.com/datasheet/differential-probes>
- [44] Yuasa, 'Yuasa NP12-6 Industrial VRLA Battery'. Accessed: Aug. 01, 2021. [Online]. Available: <https://docs.rs-online.com/5185/0900766b801b9cea.pdf>
- [45] A. J. Salkind, P. Singh, A. Cannone, T. Atwater, X. Wang, and D. Reisner, 'Impedance modeling of intermediate size lead–acid batteries', *Journal of Power Sources*, vol. 116, no. 1–2, pp. 174–184, Jul. 2003, doi: 10.1016/S0378-7753(02)00690-0.
- [46] A. Pini, 'Comprendre les principes fondamentaux des adaptateurs coaxiaux pour mieux utiliser ces composants très utiles', Dec. 29, 2020. Accessed: Aug. 01, 2021. [Online]. Available: <https://www.digikey.fr/fr/articles/understand-the-fundamentals-of-coaxial-adapters>
- [47] A. Pini, 'Understanding, Selecting, and Using Passive Oscilloscope Probes', Jul. 12, 2017. Accessed: Aug. 01, 2021. [Online]. Available: <https://www.digikey.fr/fr/articles/understanding-selecting-using-passive-oscilloscope-probes>
- [48] Tektronix, 'TPP1000 Passive probe'. Accessed: Aug. 01, 2021. [Online]. Available: <https://fr.tek.com/datasheet/passive-voltage-probes>
- [49] Tektronix, 'MSO Series 5 High-Frequency Oscilloscope'. Accessed: Aug. 01, 2021. [Online]. Available: <https://fr.tek.com/oscilloscope/5-series-mso-mixed-signal-oscilloscope>